Check for updates

View Article Online
View Journal

Nanoscale

Accepted Manuscript

This article can be cited before page numbers have been issued, to do this please use: D. Liang, U. Dahal, Y. Zhang , C. Lochbaum, D. Ray, R. Hamers, J. A. Pedersen and Q. Cui, *Nanoscale*, 2020, DOI: 10.1039/D0NR03792C.

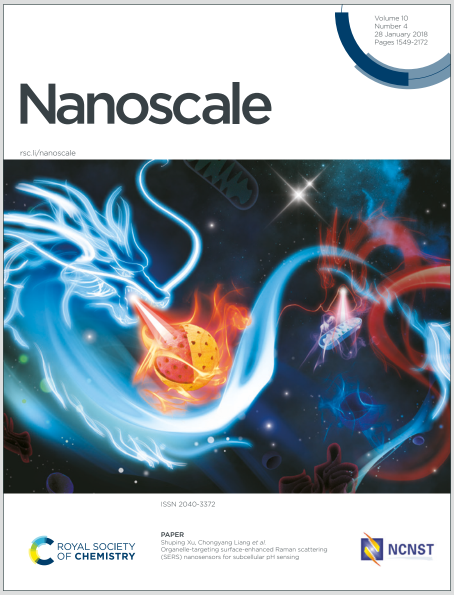

This is an Accepted Manuscript, which has been through the Royal Society of Chemistry peer review process and has been accepted for publication.

Accepted Manuscripts are published online shortly after acceptance, before technical editing, formatting and proof reading. Using this free service, authors can make their results available to the community, in citable form, before we publish the edited article. We will replace this Accepted Manuscript with the edited and formatted Advance Article as soon as it is available.

You can find more information about Accepted Manuscripts in the Information for Authors.

Please note that technical editing may introduce minor changes to the text and/or graphics, which may alter content. The journal's standard Terms & Conditions and the Ethical guidelines still apply. In no event shall the Royal Society of Chemistry be held responsible for any errors or omissions in this Accepted Manuscript or any consequences arising from the use of any information it contains.

ROYAL SOCIETY OF CHEMISTRY

rsc.li/nanoscale

View Article Online
DOI: 10.1039/D0NR03792C

Published on 21 August 2020. Downloaded by Boston University on 8/21/2020 1:44:06 PM.

Nanoscale Accepted Manuscript

Interfacial water and ion distribution determine ζ potential and binding affinity of nanoparticles to biomolecules

Dongyue Liang,[†,‡,⊥] Udaya Dahal,[‡,⊥] Yongqian (Kelly) Zhang,[†] Christian Lochbaum,[†] Dhiman Ray,[¶] Robert J. Hamers,[†] Joel A. Pedersen,[§,†] and Qiang Cui[*,‡,‖]

[†] *Department of Chemistry, University of Wisconsin-Madison, 1101 University Avenue, Madison, WI 53706*

[‡] *Department of Chemistry, Boston University, 590 Commonwealth Avenue Boston, MA 02215*

[¶] *Department of Chemistry, University of California, Irvine, 1102 Natural Sciences 2, Irvine, CA 92617*

[§] *Departments of Soil Science, Civil & Environmental Engineering, and Chemistry, University of Wisconsin-Madison, 1525 Observatory Drive, Madison, WI 53706*

[‖] *Departments of Physics and Biomedical Engineering, Boston University, 590 Commonwealth Avenue Boston, MA 02215*

[⊥] *Contributed equally to this work*

E-mail: qiangcui@bu.edu, Tel:(+1)-617-353-6189

View Article Online
DOI: 10.1039/D0NR03792C

Published on 21 August 2020. Downloaded by Boston University on 8/21/2020 1:44:06 PM.

Nanoscale Accepted Manuscript

Abstract

The molecular features that dictate interactions between functionalized nanoparticles and biomolecules are not well understood. This is in part because for highly charged nanoparticles in solution, establishing a clear connection between the molecular features of surface ligands and common experimental observables such as ζ potential requires going beyond the classical models based on continuum and mean field models. Motivated by these considerations, molecular dynamics simulations are used to probe the electrostatic properties of functionalized gold nanoparticles and their interaction with a charged peptide in salt solutions. Counterions are observed to screen the bare ligand charge to a significant degree even at the moderate salt concentration of 50 mM. As a result, the apparent charge density and ζ potential are largely insensitive to the bare ligand charge densities, which fall in the range of ligand densities typically measured experimentally for gold nanoparticles. While this screening effect was predicted by classical models such as the Manning condensation theory, the magnitudes of the apparent surface charge from microscopic simulations and mean-field models are significantly different. Moreover, our simulations found that the chemical features of the surface ligand (e.g., primary vs. quaternary amines, heterogeneous ligand lengths) modulate the interfacial ion and water distributions and therefore the interfacial potential. The importance of interfacial water is further highlighted by the observation that introducing a fraction of hydrophobic ligands enhances the strength of electrostatic binding of the charged peptide. Finally, the simulations highlight that the electric double layer is perturbed upon binding interactions. As a result, it is the *bare charge density* rather than the *apparent charge density* or ζ potential that better correlates with binding affinity of the nanoparticle to a charged peptide. Overall, our study highlights the importance of molecular features of the nanoparticle/water interface and underscores a set of design rules for the modulation of electrostatic driven interactions at nano/bio interfaces.

View Article Online
DOI: 10.1039/D0NR03792C

Published on 21 August 2020. Downloaded by Boston University on 8/21/2020 1:44:06 PM.

Nanoscale Accepted Manuscript

1 Introduction

Nanomaterials hold great promise in a broad range of applications in the area of catalysis, energy storage, imaging and nanomedicine.[1–10] To further enhance their functionality while minimizing potential negative impact on the environment or health,[11–15] it is important to understand physical and chemical factors that dictate the interaction between nanomaterials and (bio)molecules. For example, it is now well established that nanomaterials readily interact with various organic and biomolecules,[16,17] such as proteins, nucleic acids and lipids.[18] Since such interactions may further lead to damaging transformations such as disruption of lipid membranes, induction of protein conformational changes or unfolding,[19] and chemical modification of nucleic acids, it is desirable to minimize the interaction through surface functionalization of nanomaterials.[20] Similarly, adsorption of proteins on nanomaterials may interfere with the intended function, which again motivates strategies for minimizing protein corona formation.[21] On the other hand, in other applications such as targeted drug or micronutrient delivery, it is desirable to enhance interaction between the nanomaterials with specific protein receptors and/or lipids.[22,23]

The interaction between functionalized nanomaterials and (bio)molecules depends on many factors that include electrostatics, van der Waals interactions, hydrophobic effects, configurational entropy, and ion-specific effects.[20,24–29] Since most biomolecules feature highly charged surfaces, electrostatics are expected to play a major role at nano/bio interfaces. For example, previous studies found that highly charged cationic nanoparticles readily bound to lipid membranes while negatively charged nanoparticles exhibited much weaker binding[30] and toxicity towards *Daphnia magna*;[31,32] functionalizing the surface of gold nanoparticle with zwitterionic ligands rather than ligands with a net charge appeared to significantly reduce protein corona formation;[33] electrostatic interactions were found to play an important role in extraction of lipids from liposome[34]/lipid bilayer by polyelectrolyte-wrapped nanoparticles to form lipid corona;[18] and finally, cytochrome *c* was observed to mediate interactions between mercaptopropionic acid (MPA)-functionalized nanoparticle and lipid mem-

View Article Online
DOI: 10.1039/D0NR03792C

Published on 21 August 2020. Downloaded by Boston University on 8/21/2020 1:44:06 PM.

Nanoscale Accepted Manuscript

branes,[35,36] where electrostatic interactions between cationic lysine residues in cytochrome *c* and carboxylates in MPA were shown to drive their association.[37] Therefore, to control the interaction between functionalized nanomaterials and (bio)molecules, it is important to characterize nanomaterials' electrostatic properties, understand how they are modulated by functionalization (e.g., density, charge and distribution of surface ligands) and establish their relevance to the strength of binding at nano/bio interfaces.

In experimental studies, a widely used approach for characterizing electrostatic properties of colloidal and nanoparticles is electrophoresis, in which the electrophoretic mobility of the particle in the presence of a uniform external electric field is measured. The electrophoretic mobility is then used to derive the ζ potential,[38] which is generally regarded to qualitatively reflect the apparent charge density of the particle. A quantitative connection between the ζ potential and the apparent charge, as extensively discussed in the literature,[38–43] is not straightforward due to complexities in the structure and dynamics of interfacial solvent and counterions. Indeed, the connections between electrophoretic mobility, ζ potential and apparent charge are established with continuum and mean-field descriptions[44] of interfacial electrostatics (e.g., Debye-Hückel theory) and solvent dielectric and flow properties,[38,45] which may have significant limitations; for example, particles with the same charge but different degrees of structural rigidity may exhibit significantly different ζ potentials.[41] The limitations of mean-field/continuum models are expected to be particularly severe for nanoparticles, for which the scale separation between the particle and solvent/ions is not large, thus the molecular features of the particle/solvent interface can not be ignored.[46] Along the same line, the distinction between the bare charge and apparent charge is likely more complex for nanoparticles as the degree of charge compensation due to the counterions[24,25,47,48] may not be quantitatively captured with theoretical models such as the Manning condensation theory,[49–52] which ignores the molecular feature of the interface.

Another complicating factor is that the ligands used to functionalize nanomaterials often contain titratable groups, thus it is important to distinguish surface ligand density from

View Article Online
DOI: 10.1039/D0NR03792C

Published on 21 August 2020. Downloaded by Boston University on 8/21/2020 1:44:06 PM.

Nanoscale Accepted Manuscript

charge density. The relationship between surface ligand density and charge density can be complex due to the electrostatic coupling among titratable ligands, as well appreciated in the biophysics[53] and geochemical[54] communities. As we showed recently through an iterative Monte Carlo/Molecular Dynamics (MC/MD) analysis,[55] the bare surface charge density of a nanoparticle functionalized with alkyl amines depends on the ligand density in a non-monotonic fashion; the behavior of apparent surface charge due to compensation of the counterions, however, was not thoroughly analyzed. Moreover, whether it is the bare charge density or the apparent charge density that dictates the strength of binding remains to be better understood. Although one might speculate that apparent charge density is the most relevant quantity, the local electric double layer is likely perturbed significantly during the binding process, which would suggest that the bare charge density is, in fact, most relevant for binding.

To summarize, due to the molecular and dynamical features of nano/bio interfaces, especially those of interfacial solvent and counterions, prediction of the electrostatic contribution to binding affinity at such interfaces is not straightforward. To guide the design strategy to modulate electrostatically driven binding to nanoparticles, it is therefore crucial to better understand the connections among ligand properties (e.g., chemical nature and surface density, ρ_{lig}), nanoparticle features (e.g., bare vs. apparent charge densities, σ_{bare} vs. σ_{app}), experimental characterizations (electrophoretic mobility, μ, and ζ potential) and binding free energy (see Scheme 1). In so doing, we are able to identify the most impactful surface ligand properties for tuning binding affinity at nano/bio interfaces while being guided by only the most relevant experimental characterizations.

Motivated by these considerations, we develop a set of simple models for functionalized nanoparticles and study their electrokinetic and electrostatic properties using molecular simulations; we also compute the binding free energies of these nanoparticles with a charged octa-peptide (Asp$_8$), chosen because of our focus on electrostatically driven binding in this study. The results advance our understanding of the connections among key ligand features

View Article Online
DOI: 10.1039/D0NR03792C

Published on 21 August 2020. Downloaded by Boston University on 8/21/2020 1:44:06 PM.

Nanoscale Accepted Manuscript

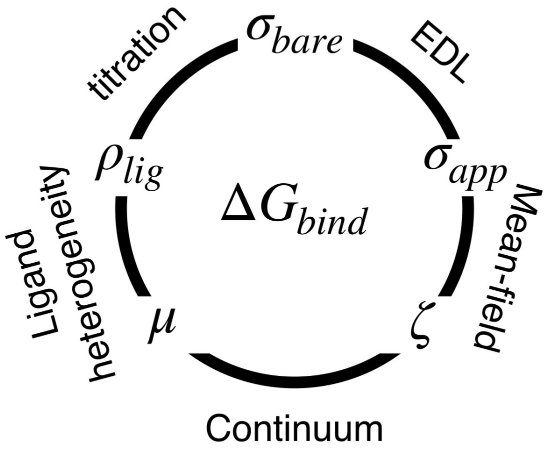

Scheme 1: Due to complicating factors such as the molecular nature of surface ligands, their titration, and response of the electric double layer (EDL) to external perturbation (e.g., binding), the relationships between surface ligand density (ρ_{lig}), bare surface charge density (σ_{bare}), apparent surface charge density (σ_{app}), electrophoretic mobility (μ) and surface electrostatic potential (ζ) are likely complex. The goal of this work is to establish among these properties, which ones are most relevant to the binding affinity of the nanoparticle to charged biomolecules.

and nanoparticle properties at a microscopic level and factors that are most predictive of the binding affinity. In particular, we aim to understand: (1) to what degree do electrophoretic mobility and ζ potential reflect the distribution and magnitude of bare or apparent charge on the nanoparticle; (2) validity of continuum models for connecting electrophoretic mobility and interfacial electrostatic potential; (3) which key ligand features and nanoparticle properties are most strongly correlated with the binding free energy, ΔG_{bind}: surface ligand density, bare charge density, apparent charge density, electrophoretic mobility and ζ potential; and (4) to what degree can we modulate ΔG_{bind} by perturbing the interfacial solvent and ion distributions through introducing non-polar surface ligands without altering the density of charged ligands? Some of the questions, especially the first two, have been explored in previous experimental[39,41,43] and theoretical/simulation[47,48,56] analyses, although rarely at a molecular level of detail.[42,57,58] In particular, we are not aware of any study that explicitly and systematically probed the question regarding binding free energy, which is the ultimate quantity of interest here.

The manuscript is organized as follows. We first briefly review electrokinetic properties

View Article Online
DOI: 10.1039/D0NR03792C

Published on 21 August 2020. Downloaded by Boston University on 8/21/2020 1:44:06 PM.

Nanoscale Accepted Manuscript

of nanoparticles and summarize computational models and simulation details. Next, we present the interfacial properties (e.g., ion distribution and electrostatic potential profile) of the nanoparticles, followed by the analysis of apparent charge and ζ potential. Then, we discuss the binding free energies of the charged peptide to different nanoparticles. We end with a summary of the key findings along with several concluding remarks.

2 Theoretical and Computational Methods

2.1 A Brief Review of Electrokinetic Properties and Analysis

As discussed in Introduction, electrophoresis measurement[38] is widely used to characterize the electrostatic properties (e.g., apparent charge) of colloidal and nanoparticles.[39,41,59] The electrostatic force balances with the frictional force and retardation force from the medium, leading to a constant drift velocity, v; the electrophoretic mobility is simply defined as the ratio of drift velocity to the applied external electric field strength (E),

$$\mu = \frac{v}{E}. \tag{1}$$

Continuum theories[38,40,45] were developed to connect electrophoretic mobility with the electrostatic potential at the "slipping plane", where the solvent velocity relative to the drifting particle vanishes. The relationship is usually cast in the form of the Smoluchowski theory,[44]

$$\mu = \frac{2}{3} H(\kappa a) \frac{\epsilon_r \epsilon_0 \zeta}{\eta}, \tag{2}$$

where η and ϵ_r are the dynamic viscosity and dielectric constant of the solvent medium, and ϵ_0 is the vacuum permittivity. The Henry's function,[60] $H(\kappa a)$, is a factor dependent on the ratio of particle radius (a) and Debye length ($\lambda_D = \kappa^{-1}$) and takes a value between 1 and 3/2, where 1 and 3/2 lead to the Hückel and Smoluchowski limit, respectively.

Gouy-Chapman and Debye-Hückel models[25] are widely applied to further link ζ poten-

View Article Online
DOI: 10.1039/D0NR03792C

Published on 21 August 2020. Downloaded by Boston University on 8/21/2020 1:44:06 PM.

Nanoscale Accepted Manuscript

tial to an apparent surface charge density. The Gouy-Chapman model adopts a Poisson-Boltzmann description of counterions near a planar, rigid surface; it assumes that the diffuse counterions in solution follow Boltzmann statistics without explicit ion-ion correlation, along with a continuum description of the (water) solvent. The Debye-Hückel approximation further simplifies the expression by assuming that the potential variation is small, which is valid at very low ionic strength and low charge density. The relation between the apparent charge density (σ_{app}) at the slipping plane and ζ potential is given as,[25]

$$\sigma_{app} = \sqrt{8cN_A\epsilon_r\epsilon_0k_BT}sinh\left(\frac{e\zeta}{2k_BT}\right), \tag{3}$$

where c is the ionic concentration, and N_A is Avogadro's number. Another expression commonly used for particle of radius a is,[61]

$$\sigma_{app} = \frac{\epsilon_r\epsilon_0k_BT}{a}\zeta(1+\kappa a). \tag{4}$$

Following Eqns. 1-4, the apparent charge density at the slipping plane of charged nanoparticles can be estimated experimentally by electrophoresis measurement within the framework of continuum and mean-field models.

2.2 Computational Models and Simulation Details

We focus on a spherical gold nanoparticle of 2 nm diameter (which contains 240 Au atoms) functionalized with different sets of alkyl amines; the surface ligand density is 5.2 nm^{-2}, comparable to that characterized in experiments for gold nanoparticles of similar size,[62] leading to 65 ligands on the surface. To test the impact of the core structure, we have also studied a model similar to that characterized experimentally in recent work;[63] it contains 296 Au atoms and 84 ligands on the surface, and features the Au-S staple motifs discussed in previous studies.[63–65] For ligands, both primary and quaternary amines of different protonation states are explored. In total, ten nanoparticles (some of which are illustrated in Fig. 1)

View Article Online
DOI: 10.1039/D0NR03792C

Published on 21 August 2020. Downloaded by Boston University on 8/21/2020 1:44:06 PM.

Nanoscale Accepted Manuscript

are designed to explore different ligand features, and their compositions and notations are summarized in Table 1. C4P65 and C4N65 have all the butyl amines protonated and deprotonated, respectively. In C4P32-C4N33 (Fig. 1c), approximately 50% of the butyl amines (randomly selected) is protonated while the rest deprotonated; this setup is motivated by our recent study,[55] which showed that under neutral pH condition and the current ligand density, only 50% of the butyl amines is expected to be protonated. To explore the effect of ligand heterogeneity, which was shown[55] to enhance the bare charge due to a decrease in the electrostatic coupling between titratable groups, we also study C8P32-C4P33 (Fig. 1d), in which protonated butyl and octyl amines are randomly mixed on the surface. In addition, we also study C4Q65 (Fig. 1e), which features quaternary amines, to explore the impact of chemical detail of charged ligands on the electrostatic properties (e.g., ζ potential) and binding free energy. In the C4P32-C4C33 system, we mix protonated butyl amine and pentyl ligands to investigate the effect of mixing charged and non-polar ligands; compared to C4P32-C4N33, replacing the neutral amine (C4N) with an alkyl ligand (C4C) maintains the same bare charge density but perturbs the interfacial solvent/ion distributions. Finally, to further confirm the differences between primary and quaternary amines and the impact of mixing charged/neutral ligands, we also study two additional mixed-ligand particles: C4Q32-C4C33, which mixes quaternary butyl amines and pentyl ligands, and C4Q32-C4M33, which mixes quaternary butyl amines and butyl methyl ether.

Equilibrium and non-equilibrium molecular dynamics simulations are carried out to study the electrostatic properties of all nanoparticles. In each case, the nanoparticle is solvated in a 12 nm length cubic box, and NaCl is added with the displacement method to the desired concentration using the SLTCAP protocol[66] for number estimations (see Fig. 2a for an illustration). Equilibrium simulations are used to estimate the apparent charge and microscopic electrostatic profiles at two salt concentrations, 50 mM and 150 mM. The CHARMM36 force field[67–69] with NBFIX corrections for the ions[70] is used to treat the alkyl amine ligands, water and ions. The INTERFACE force field[71] is used for the gold atoms, which are charge

View Article Online

DOI: 10.1039/D0NR03792C

Published on 21 August 2020. Downloaded by Boston University on 8/21/2020 1:44:06 PM.

Nanoscale Accepted Manuscript

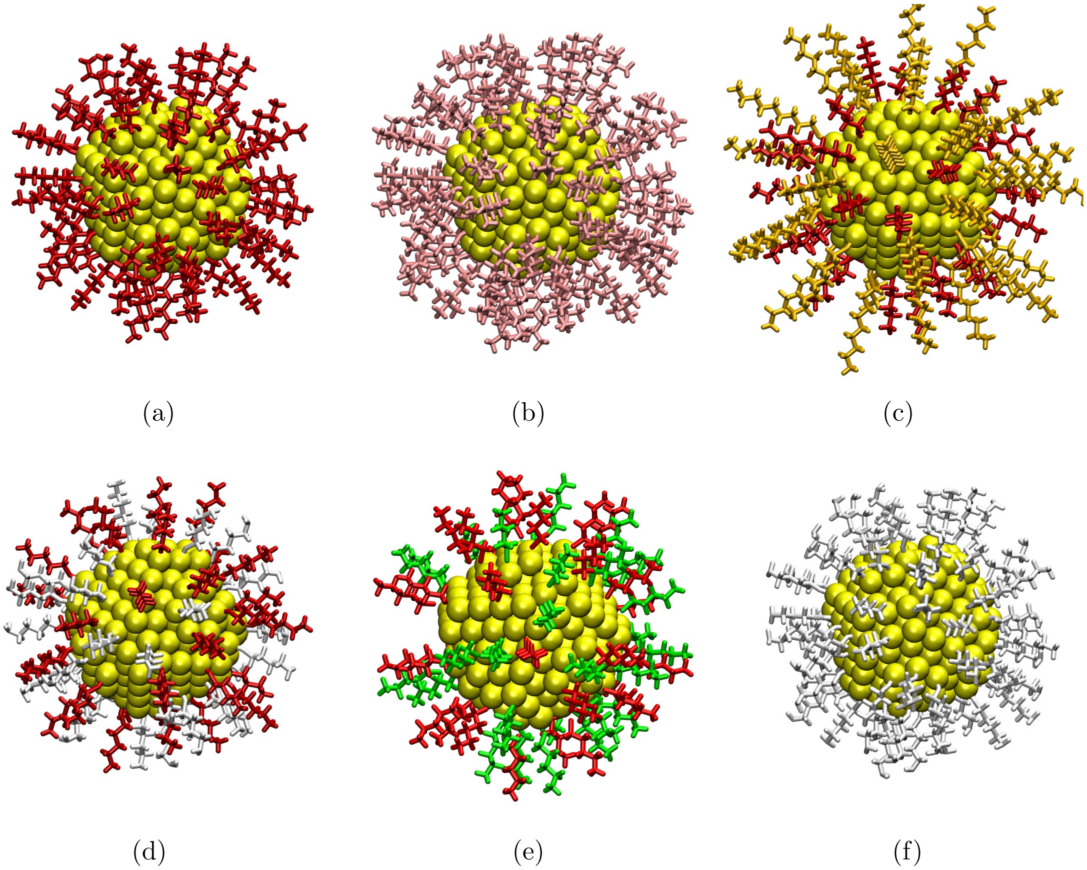

(a) (b) (c)

(d) (e) (f)

Figure 1: An illustration of selected nanoparticles studied in this work: 2-nm-diameter Au nanoparticles functionalized with 65 thiol ligands: (a) C4P65, (b) C4Q65, (c) C8P32-C4P33, (d) C4P32-C4N33, (e) C4P32-C4C33, (f) C4N65. C4P65 denotes that the nanoparticle is functionalized with 65 butyl primary amine (C4P) ligands (see Table 1 for the chemical formula for different ligands and different nanoparticles), and the rest follows the same style of nomenclature; for example, C8P32-C4P33 means 32 octyl primary amine (C8P) and 33 butyl primary amine (C4P) ligands; the total bare ligand charges are 65 for (a-c), 32 for (d-e) and 0 for (f). Four additional particles (see Table 1) are not shown. Color coding: Gold - yellow, C4P - red, C4Q - pink, C8P - orange, C4N - white, C4C - green.

View Article Online
DOI: 10.1039/D0NR03792C

Published on 21 August 2020. Downloaded by Boston University on 8/21/2020 1:44:06 PM.

Nanoscale Accepted Manuscript

Table 1: Model ligands and nanoparticles explored in this study

Model ligand[a]	Chemical formula	Nanoparticle [b]	Chemical formula
C4P	$\text{-S(CH}_2)_4\text{NH}_3^+$	C4P65	$\text{Au}_{240}\ [\text{S(CH}_2)_4\text{NH}_3^+]_{65}$
C4Q	$\text{-S(CH}_2)_4\text{N(CH}_3)_3^+$	C4Q65	$\text{Au}_{240}\ [\text{S(CH}_2)_4\text{N(CH}_3)_3^+]_{65}$
C8P	$\text{-S(CH}_2)_8\text{NH}_3^+$	C8P32-C4P33	$\text{Au}_{240}\ [\text{S(CH}_2)_8\text{NH}_3^+]_{32}[\text{S(CH}_2)_4\text{NH}_3^+]_{33}$
C4N	$\text{-S(CH}_2)_4\text{NH}_2$	C4Q32-C4C33	$\text{Au}_{240}\ [\text{S(CH}_2)_4\text{N(CH}_3)_3^+]_{32}\ [\text{S(CH}_2)_4\text{CH}_3]_{33}$
C4C	$\text{-S(CH}_2)_4\text{CH}_3$	C4Q32-C4M33	$\text{Au}_{240}\ [\text{S(CH}_2)_4\text{N(CH}_3)_3^+]_{32}\ [\text{S(CH}_2)_4\text{OCH}_3]_{33}$
C4M	$\text{-S(CH}_2)_4\text{OCH}_3$	C4P32-C4N33	$\text{Au}_{240}\ [\text{S(CH}_2)_4\text{NH}_3^+]_{32}\ [\text{S(CH}_2)_4\text{NH}_2]_{33}$
–	–	C4P32-C4C33	$\text{Au}_{240}\ [\text{S(CH}_2)_4\text{NH}_3^+]_{32}\ [\text{S(CH}_2)_4\text{CH}_3]_{33}$
–	–	C4N65	$\text{Au}_{240}\ [\text{S(CH}_2)_4\text{NH}_2]_{65}$
–	–	C4P84 [c]	$\text{Au}_{279}\ [\text{S(CH}_2)_4\text{NH}_3^+]_{84}$
–	–	C4P42-C4N42 [c]	$\text{Au}_{279}\ [\text{S(CH}_2)_4\text{NH}_3^+]_{42}\ [\text{S(CH}_2)_4\text{NH}_2]_{42}$

a. The notation C4/C8 refers to the chain length of the alkyl linker; "P" and "Q" indicate primary and quaternary amines, respectively; "N" indicates a deprotonated primary amine, "C" indicates a methyl as the terminal group, and "M" indicates a methyl ether as the terminal group.

b. For an illustration of some of the functionalized gold nanoparticles, see Fig. 1.

c. For results for C4P84, C4P42-C4N42, which contain a different core structure, see Sect. 4 of **Supporting Information**; in general, the key trends observed in this study are not sensitive to the core structure of the nanoparticle.

neutral. This combination was found adequate for describing the ligand behavior at the gold/water interface by a systematic set of QM, QM/MM and MM comparisons.[72] To ensure the structural integrity of the nanoparticle, especially in drift velocity simulations, each gold atom is bonded to all its nearest neighbors as in the crystal structure using a covalent bond with a force constant of 1000 $\text{kcal}\cdot\text{mol}^{-1}\cdot\text{Å}^{-2}$. NAMD 2.12[73] with GPU acceleration is used for all the simulations unless stated otherwise. Particle-mesh-Ewald[74] is applied to calculate electrostatic interactions with a grid size of 128 for each direction. A switching function is applied to treat van der Waals interactions with a switching distance of 1.0 nm and a cutoff distance of 1.2 nm. The RATTLE algorithm[75] is applied to constrain all bonds involving hydrogen in the simulation. The temperature is maintained at 300K using the Langevin thermostat[76] with a damping coefficient of 1 ps^{-1} in the equilibrium simulations, and the integration time step is 2.0 fs. Each system is first equilibrated under the NPT ensemble using the Langevin pressure control[77] with a target pressure of 1.01325 bar, and production runs (>80 ns) are performed with the NVT ensemble (see Fig. S1 for test of convergence).

View Article Online
DOI: 10.1039/D0NR03792C

Published on 21 August 2020. Downloaded by Boston University on 8/21/2020 1:44:06 PM.

With non-polarizable force fields such as CHARMM36, the issue of over-binding of counterions to charged groups has been discussed especially for multi-valent ions.[78] To understand the impact of including electronic polarization on the electrostatic properties of nanoparticles in salt solution, we also conduct simulations for the C4P65 system with a NaCl concentration of 150 mM using the CHARMM-Drude force field.[79–81] The Drude system is identical to the non-polarizable system in terms of composition, and the conversion from the latter to the Drude model is done using scripts from the Drude builder module of CHARMM-GUI.[82] For simplicity, only the ligands, water molecules and ions are converted to polarizable models, keeping the gold non-polarizable. This is appropriate for the current purpose because analysis of ion distribution around the nanoparticle clearly indicates that the gold core is inaccessible to the ions; similarly, the peptide Asp_8 also mainly interact with the surface ligands.

To simulate the electrophoresis process, non-equilibrium simulations are carried out to compute drift velocity as discussed in previous work[58,70] for the systems with 150 mM salt solution using the non-polarizable force field. In the drift velocity simulation, a constant electric field of $0.05\ \text{kcal} \cdot \text{mol}^{-1} \cdot \text{Å}^{-1} \cdot \text{e}^{-1}$ ($1\ \text{kcal} \cdot \text{mol}^{-1} \cdot \text{Å}^{-1} \cdot \text{e}^{-1} = 4.3 \times 10^6$ V/cm, referred to as the "NAMD unit" thereafter) is applied to all atoms in the system, and the electrophoretic mobility of the nanoparticle is evaluated following Eqn. 1. We note that while the magnitude of the electric field used here is rather low compared to previous studies (which used ∼0.8 NAMD unit[58] or 0.07-1.2 NAMD unit[83]), it is orders of magnitude higher than that used in realistic experiments. Analysis of the counterion distributions around the nanoparticle (Fig. S9) suggest that the electric double layer is not significantly perturbed at the chosen electric field; moreover, at lower fields (e.g., 0.025 NAMD unit), uncertainty in the estimated drift velocity increases due to diffusion of the nanoparticle (Fig. S11). Thus, the value of 0.05 NAMD unit is selected as the best balance between perturbation of the electric double layer and uncertainty in the estimated drift velocity. For the non-equilibrium drift velocity simulations, most of the simulation parameters are consistent with

Nanoscale Accepted Manuscript

View Article Online
DOI: 10.1039/D0NR03792C

Published on 21 August 2020. Downloaded by Boston University on 8/21/2020 1:44:06 PM.

Nanoscale Accepted Manuscript

the equilibrium simulations except for the Langevin damping coefficient. Comparison to Nosé-Hoover thermostat shows a damping coefficient smaller than 0.02 ps^{-1} being necessary for obtaining the correct drift velocity with the electric field applied (see SI for detail). For each system, six independent runs (>80 ns each) are performed to estimate the statistical uncertainty of the computed mobilities (Fig. S10).

Finally, to compute the binding free energy between nanoparticles and Asp_8, umbrella sampling with the weighted histogram analysis method[84] (WHAM) is conducted using the non-polarizable force field. The reaction coordinate is the centers of mass separation between the gold nanoparticle and the peptide. The reaction coordinate is sampled with a separation of 0.1 nm between neighboring windows and at least 30 windows are simulated for each system depending on the convergence of the computed potential of mean force (PMF). Each window is sampled for at least 10 ns and the statistical error analysis for the PMF is conducted using cumulative block averaging.[85] To probe the effect of peptide charge on the trends in binding affinity, umbrella sampling simulations have also been conducted for Asp_8 in which the sidechains adopt alternating protonation states, leading to a reduced total charge of -4. The results are shown in Sect. 3 of the **Supporting Information**.

3 Results and Discussions

3.1 General Trends in Counterion Distribution and Interfacial Potential

To elucidate counterion distribution around a nanoparticle in salt solution, radial distribution functions (RDFs) of chloride ions (Cl^-) with respect to the nanoparticle center from the equilibrium molecular dynamics simulations are shown in Fig. 2b and Fig.S2. For all the charged particles, the RDF shows a single peak at around 15 Å including the particle functionalized with ligands featuring two different non-polar (butyl and octyl) chain lengths. This is consistent with the nanoparticle center – ligand nitrogen number densities in Fig.

Published on 21 August 2020. Downloaded by Boston University on 8/21/2020 1:44:06 PM.

Nanoscale Accepted Manuscript

S3, which show little difference in peak positions among the different cases, suggesting that the longer amine ligands are flexible and adopt bent configurations. At both salt concentrations, the peak height of the RDF generally follows the order of the total bare charge (e.g., C4P65>C4P32-C4N33) and the height is larger for primary amines than quaternary amines (e.g., C4P65>C4Q65), as expected based on the less favorable interaction between Cl^- with the methyl groups in the quaternary amines. Mixing of primary amines of different chain length (C8P32-C4P33) leads to lower Cl^- correlation, due to the fact some of the butyl amines are blocked by the octyl amines from accessing Cl^- ions. In other cases of mixed-ligand nanoparticles, the Cl^- RDF is not sensitive to the identity of the charge-neutral ligand (C4N, C4C, C4M). For all cases with charged ligands, a high degree of counterion compensation is observed, which is discussed quantitatively in the next subsection. For the neutral nanoparticle (C4N65), no obvious peak is observed in the chloride RDF, as expected.

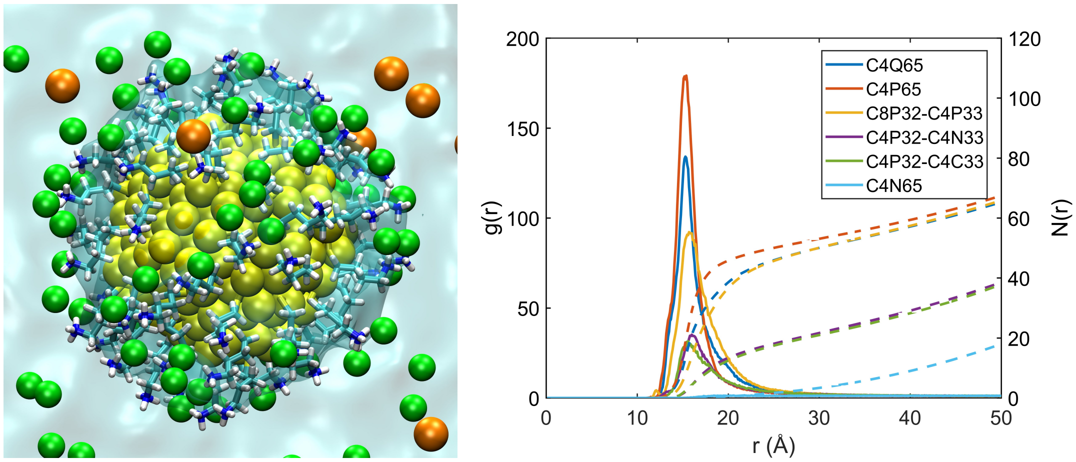

(a) (b)

Figure 2: Chloride ion distribution around functionalized nanoparticles. (a) An illustration of the ion distribution around a C4P65 nanoparticle. Water molecules are shown in the QuickSurf representation, color coding: Au - yellow, C - cyan, N - blue, Cl - green, Na - orange. (b) Radial distribution function of chloride ions with respect to the nanoparticle center at 50 mM NaCl for the nanoparticles shown in Fig. 1; the dashed lines are integrated radial distribution functions. For results for the remaining particles (C4Q32-C4C33, C4Q32-C4M33) and results for 150 mM NaCl, see Fig.S2.

To analyze the electrostatic potential (ESP) profile near the nanoparticle, we assume

View Article Online
DOI: 10.1039/D0NR03792C

Published on 21 August 2020. Downloaded by Boston University on 8/21/2020 1:44:06 PM.

Nanoscale Accepted Manuscript

angular homogeneity and calculate the ESP as a function of the radial distance from the nanoparticle center using Gauss's Law.[86] The expression of the radial electric field is,

$$E\left(r\right) = \frac{1}{4\pi r^2 \epsilon_0} \int_0^r dr' 4\pi r'^2 \rho\left(r'\right), \tag{5}$$

in which $\rho(r')$ is the cumulative charge density obtained from equilibrium MD simulations. The ESP is then obtained by radial integration,

$$\phi\left(r\right) = \int_r^\infty dr' E\left(r'\right), \tag{6}$$

with the bulk value set to 0.

The calculated ESP profiles at the two salt concentrations are shown in Fig. 3 and Fig. S4. The ESP in all the cases features a range of approximately 1 V from the center of the particle relative to the bulk region. Overall, the interfacial (r ~20 Å) ESP values are higher for the lower (50 mM) salt simulations (compare Fig. 3b and Fig. S4b, for example), as expected based on the consideration of salt screening of surface charge, although at each salt concentration, the interfacial ESP values do not simply follow the order of total bare ligand charge (*vide infra*). Between the region of 10 and 20 Å, the ESP profiles show non-monotonic behavior with an overall decreasing trend. For most of the cases studied, the profiles go below the bulk value at certain distance and this is most obvious for the C4N65 and C4Q65 cases. Such "charge inversion" behavior in the ESP profile was also observed in our previous work on functionalized model carbon nanoparticle.[55] These features of the ESP profiles highlight that the identification of the "slipping plane" is crucial to the estimate of ζ potential at the microscopic level, which is discussed in the next subsection in more detail.

To probe the impact of including electronic polarization, we compare results from simulations using CHARMM36 and the Drude force field (see Fig. 4). The chloride-nanoparticle RDF obtained with the Drude model exhibits lower and broader peaks compared to result with the non-polarizable force field, although the difference in the integrated RDF is modest.

View Article Online
DOI: 10.1039/D0NR03792C

Published on 21 August 2020. Downloaded by Boston University on 8/21/2020 1:44:06 PM.

Nanoscale Accepted Manuscript

The ESP profile from the Drude model is generally similar to that using the non-polarizable force field, especially at radial distances larger than 15 Å; it also exhibits the ESP inversion near the particle/water interface as observed with the non-polarizable force field. Overall, the results confirm that inclusion of electronic polarization does not significantly impact the ion distribution and ESP profiles around the charged nanoparticle despite the relatively high bare charge density; this is reassuring, in line with the consideration that electronic polarization is more significant for multivalent ions.

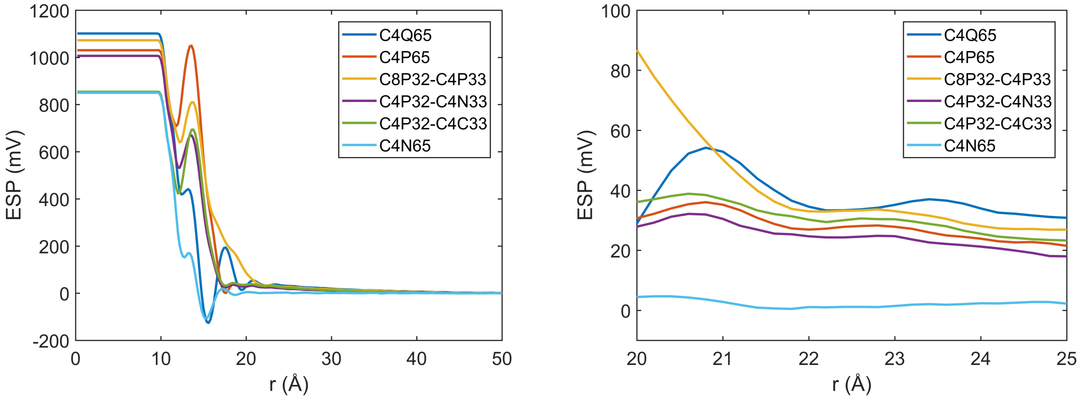

(a) (b)

Figure 3: Computed electrostatic potential (ESP) as a function of distance from the nanoparticle center at NaCl concentration of 50 mM for the nanoparticles shown in Fig. 1. Panel (a) shows the overall profile, while panel (b) enlarges the interfacial region. For results for the remaining particles (C4Q32-C4C33, C4Q32-C4M33) and results for 150 mM NaCl, see Fig.S4.

3.2 Apparent Charge of Nanoparticle

To obtain a microscopic estimate of the apparent charge and ζ potential of the nanoparticles, we attempt to identify the boundary between the bound and diffuse ions; this is more straightforward than monitoring the solvent flow around the nanoparticle because it can be done with equilibrium simulations. We fit the tail part of the RDFs shown in Fig. 2 to the Debye-Hückel expression of counterion distribution near a spherical particle, $A^{-Br}/r + C$. Since Debye-Hückel is only valid for the diffuse layer of counterions, the location where the

View Article Online
DOI: 10.1039/D0NR03792C

Published on 21 August 2020. Downloaded by Boston University on 8/21/2020 1:44:06 PM.

Nanoscale Accepted Manuscript

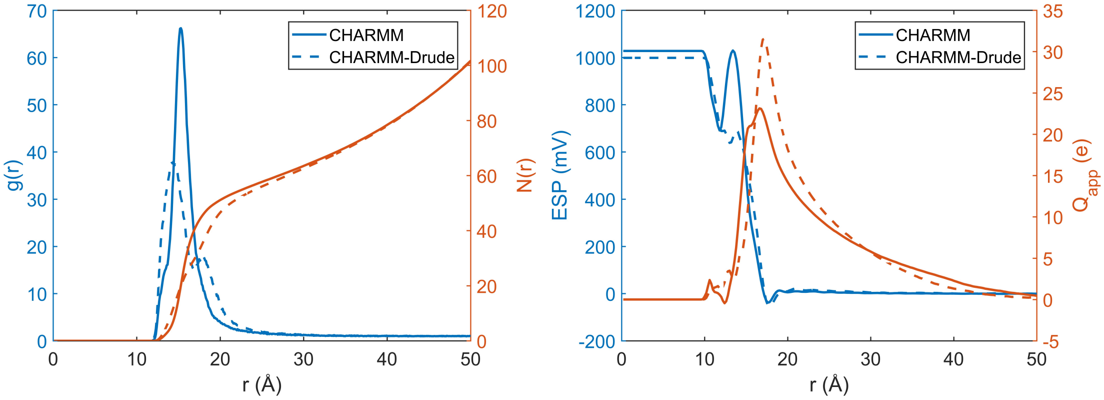

(a) (b)

Figure 4: Comparison of (a) chloride distribution and (b) electrostatic potential with respect to the C4P65 nanoparticle center at NaCl concentration of 150 mM from MD simulations with non-polarizable and polarizable (Drude) CHARMM force fields. In (a), $g(r)$ is the chloride radial distribution function with respect to the nanoparticle center, and $N(r)$ is the integrated radial distribution function. Also shown in (b) is the magnitude of apparent nanoparticle charge (Q_{app}) as a function of distance to the nanoparticle center, which is the sum of ligand charge and counterion charge.

simulated RDFs start to deviate from the analytical Debye-Hückel expression is identified as the boundary of the diffuse layer and also the "slipping plane" (i.e., r_{slip}). As shown in Fig. S5, the result of fitting is somewhat sensitive to the range of radial distances included; thus for each RDF, we average over multiple fittings with different ranges of radial distances as a way to estimate the uncertainty in the location of the slipping plane (also summarized in Table 2). When such uncertainty is considered, the difference in r_{slip} for different nanoparticles at a given salt concentration is relatively modest, mostly within the range of uncertainty.

The apparent charge of the nanoparticle in salt solution (shown in Table 2) is calculated as the sum of the bare charge carried by the nanoparticle and the compensating ions within the slipping plane. At the same salt concentration, the difference in the apparent charge among different nanoparticles is evident but modest, when uncertainly due to the range of the slipping plane location is taken into consideration, highlighting the significant contribution from the counterions. For example, for C4P65 and C4P32-C4N33/C4P32-C4C33 nanoparticles, which differ in bare charge by a factor of two, the apparent charges are sta-

View Article Online
DOI: 10.1039/D0NR03792C

Published on 21 August 2020. Downloaded by Boston University on 8/21/2020 1:44:06 PM.

Nanoscale Accepted Manuscript

Table 2: Bare charge Q_{bare} and apparent charge $Q_{app}(r_{slip})$ of functionalized gold nanoparticles obtained at the estimated slipping plane $(r_{slip})^a$ from the radial apparent charge profile in Fig. 5.

Nanoparticle	Q_{bare}	50 mM NaCl		150 mM NaCl	
		r_{slip} (Å)	$Q_{app}(r_{slip})$ (e)	r_{slip} (Å)	$Q_{app}(r_{slip})$ (e)
C4Q65	65	23.2 ± 1.0	21.2 ± 1.3	22.5 ± 0.8	17.1 ± 1.7
C4P65	65	23.3 ± 1.3	16.2 ± 1.0	22.0 ± 0.8	10.9 ± 1.0
C8P32-C4P33	65	25.1 ± 1.2	19.3 ± 1.3	23.5 ± 0.8	15.5 ± 1.5
C4Q32-C4C33	32	23.3 ± 1.1	18.7 ± 1.3	22.6 ± 1.2	14.9 ± 2.3
C4Q32-C4M33	32	23.2 ± 1.3	19.1 ± 1.5	23.1 ± 1.2	15.2 ± 2.2
C4P32-C4N33	32	22.8 ± 0.8	15.8 ± 0.7	23.2 ± 1.7	10.1 ± 2.4
C4P32-C4C33	32	22.2 ± 0.8	14.8 ± 0.7	23.1 ± 1.4	11.3 ± 2.1
C4P65 - Drude	65	–	–	23.2 ± 1.2	11.6 ± 1.9
Manning^b		–	5.5	–	1.2

a. The location of the slipping plane is identified by fitting the chloride ion RDF tails to the Debye-Hückel expression; see text and Fig. S5 for the estimated uncertainty in r_{slip}. The uncertainty in $Q_{bare}(r_{slip})$ is estimated based on the computed apparent charges over the range of estimated r_{slip} values. b. Result from the Manning condensation theory.[51] The radius of the particle is taken to be 1.45 nm based on the ligand distribution function in Fig. S3.

tistically indistinguishable due to counterion compensation. This is qualitatively consistent with Manning condensation theory,[50,51] which predicts the same apparent charge of spherical particles carrying different bare charges once the latter exceed the value $-\frac{e(1+\kappa a)ln(\kappa l_B)}{2\pi l_B a}$; κ is the inverse Debye length, l_B the Bjerrum length and a the radius of the particle. However, the Manning condensation theory predicts an apparent charge of 5.5 and 1.2 e at 50 mM and 150 mM salt, respectively, for the particles studied here (see Table 2), which differ significantly from the microscopic simulations (*vide infra*).

A closer examination of the $Q_{app}(r_{slip})$ values for the nanoparticles studied here (see Table 2) reveals several trends. First, due to less favorable chloride binding, the quaternary amine ligands lead to less counterion compensation and therefore a higher apparent charge compared to the primary amine ligands; e.g., this is evident from comparisons between C4Q65 and C4P65 and between C4Q32-C4C33 and C4P32-C4C33. Second, mixing ligands of different length in the case of C8P32-C4P33 leads to less counterion correlation with buried C4P amines (as seen in the Cl^- RDF in Fig. 2b) and therefore a high apparent charge between the values of C4P65 and C4Q65. For other mixed-ligand cases, since the chloride

View Article Online
DOI: 10.1039/D0NR03792C

Published on 21 August 2020. Downloaded by Boston University on 8/21/2020 1:44:06 PM.

Nanoscale Accepted Manuscript

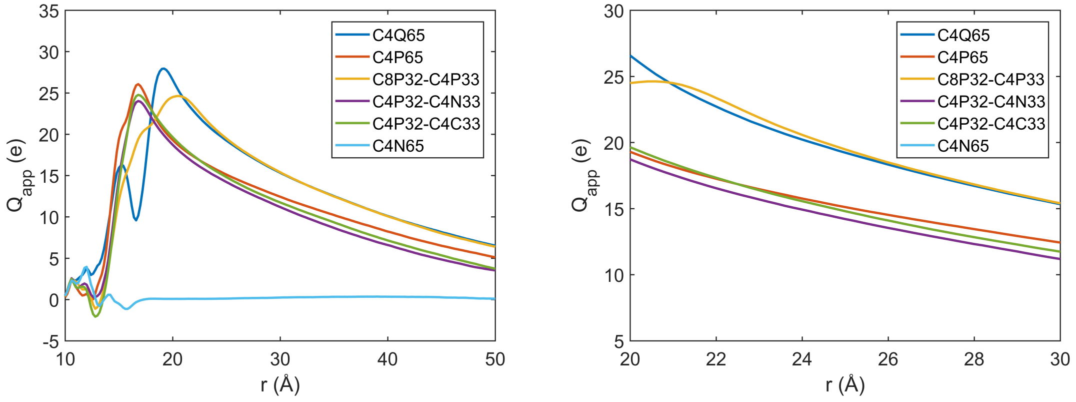

(a) (b)

Figure 5: Computed apparent charge ($Q_{app}(r)$) profiles as functions of distance from the nanoparticle center at NaCl concentration of 50 mM for the nanoparticles shown in Fig. 1; $Q_{app}(r)$ includes bare ligand charges and counterion charges up to distance r. Panel (a) shows the overall profile, while panel (b) enlarges the interfacial region. For results for the remaining particles (C4Q32-C4C33, C4Q32-C4M33) and results for 150 mM NaCl, see Fig.S6.

distribution is insensitive to the nature of the neutral ligands (Fig. 2b), the apparent charges of these nanoparticles are also sensitive to only the nature of the charged group (i.e., C4Q vs. C4P), not to the charge neutral group (C4C, C4N or C4M). Finally, the apparent charge for C4P65 from simulations with the Drude model is also listed in Table 2 for comparison, and the result shows no significant difference from that with the non-polarizable force field, as expected based on the overall similarity in the ion distributions between the two models.

3.3 Electrophoretic Mobility and Different Estimates of ζ Potentials

We apply the drift velocity protocol to calculate the electrophoretic mobility of the nanoparticles in 150 mM salt solution, along with several systems in 50 mM NaCl solution. The mobilities calculated from individual runs are summarized in Table S2, and the average values are shown in Table 3. The C4N65 nanoparticle does not drift under an electric field, as expected for a charge neutral nanoparticle. For the four charged nanoparticles studied, the

View Article Online
DOI: 10.1039/D0NR03792C

Published on 21 August 2020. Downloaded by Boston University on 8/21/2020 1:44:06 PM.

Nanoscale Accepted Manuscript

difference in mobility in 150 mM NaCl is modest, and only C4Q65 differs statistically from C4P65; the difference between the latter two is reproduced for the 50 mM NaCl condition. The different mobilities between C4Q65 and C4P65 is consistent with the observation that their apparent charges are significantly different (Table 2). On the other hand, the mixed-ligand system C8P32-C4P33 also has notably higher apparent charge than C4P65, yet the computed mobility is not significantly different; moreover, while C4P32-C4C33 carries a similar apparent charge as C4P65, its computed mobility is statistically higher. Therefore, electrophoretic mobility does not always reflect the apparent charge of a nanoparticle in salt solutions, and molecular features of the nano/particle interface such as ligand layer roughness and solvent distributions also contribute.[39]

Table 3: Computed electrophoretic mobility of nanoparticles from drift velocity simulations. Unit: $10^{-4} \cdot cm^2 \cdot V^{-1} \cdot s^{-1}$

Nanoparticle	50 mM NaCl	150 mM NaCl
C4Q65	13.1 ± 0.5	9.2 ± 0.4
C4P65	11.0 ± 0.6	7.5 ± 0.9
C8P32-C4P33	-	8.7 ± 0.9
C4P32-C4N33	-	9.0 ± 1.0
C4P32-C4C33	-	9.9 ± 0.9
C4N65	-	-0.1 ± 0.8

The electrostatic potential at the slipping plane identified as described above (r_{slip}) is termed as "microscopic ζ potential, ζ_{ESP}" and summarized in Table 4. We note that at the slipping plane, the ESP profile in all cases has reached the region of slow decay, thus no negative ζ potential is observed despite the inversion of ESP at the nanoparticle/water interface (Fig. 3b). As expected, the salt concentration has a major impact on the overall magnitude of the interfacial potential; going from 50 mM to 150 mM salt, ζ_{ESP} drops by about a factor of 2-3 in all cases studied here. At high (150 mM) salt concentration, the difference in ζ_{ESP} is generally modest and the values are all around 8-10 mV. At lower (50 mM) salt concentration, the differences are more pronounced and ζ_{ESP} spans a range of almost 10 mV (from 24 to 35 mV). In most cases, ζ_{ESP} follows the same trend as $Q_{app}(r_{slip})$;

View Article Online
DOI: 10.1039/D0NR03792C

Published on 21 August 2020. Downloaded by Boston University on 8/21/2020 1:44:06 PM.

Nanoscale Accepted Manuscript

for example, the potential is higher for particles functionalized with quaternary amines than with primary amines. A notable exception is for C4P32-C4C33, whose $Q_{app}(r_{slip})$ is comparable to C4P32-C4N33 and C4P65 but exhibits a substantially higher ζ_{ESP} value. Since $Q_{app}(r_{slip})$ considers only contributions from the bare ligand charge and counterions within the slipping plane, this observation highlights that interfacial water molecules also contribute to the interfacial electrostatic potential. In fact, this is consistent with the observation that while the apparent surface *charge* from the Manning condensation theory deviates considerably from $Q_{app}(r_{slip})$ (see Table 2), the predicted interfacial *potential* from the Manning theory[51] is in good agreement with ζ_{ESP} (see Table 4).

Table 4: ζ potentials estimated from electrostatic potential profiles $(\zeta_{ESP})^a$ and mobilities calculated from drift velocity $(\zeta_{mob})^b$ simulations.

Nanoparticle	50 mM NaCl		150 mM NaCl	
	ζ_{ESP} (mV)	ζ_{mob} (mV)	ζ_{ESP} (mV)	ζ_{mob} (mV)
C4Q65	35 ± 2.7	44 ± 1.7	10 ± 1.8	31 ± 1.3
C4P65	26 ± 2.8	37 ± 2.9	9 ± 1.2	26 ± 2.9
C4P65 - Drude	-	-	14 ± 1.1	-
C8P32-C4P33	26 ± 2.5	-	9 ± 1.4	29 ± 3.1
C4Q32-C4C33	32 ± 1.2	-	9 ± 2.3	-
C4Q32-C4M33	29 ± 2.3	-	11 ± 2.2	-
C4P32-C4N33	24 ± 1.4	-	7 ± 1.4	31 ± 3.6
C4P32-C4C33	31 ± 1.3	-	9 ± 1.3	34 ± 3.1
Manning [c]	34		5	

a. Measured at the location of the slipping plane (r_{slip}, summarized in Table 2), which is identified by fitting the chloride ion RDF tails to the Debye-Hückel expression; see text and Fig. S5 for the estimated uncertainty in r_{slip}. b. Computed based on Eq. 2 in the Smoluchowski limit. A dielectric constant of 100 and a viscosity of 0.3 mPa·s computed for TIP3P is applied.[87] c. Result from the Manning condensation theory.[51]

For cases where the mobility is computed, the ζ potential is also estimated with Eqn. 1, and the results are summarized in Table 4 as ζ_{mob} for comparison with ζ_{ESP}. In general, ζ_{mob} values are substantially higher than ζ_{ESP}, especially at the high salt concentration. Since ζ_{mob} is linearly proportion to μ, the trend follows that in the mobility, which is that the only statistically significant differences are between C4P65 and C4Q65/C4P32-C4C33, with the latter two having notably higher ζ_{mob}. For additional discussions, see Subsect. 3.5.

View Article Online
DOI: 10.1039/D0NR03792C

Published on 21 August 2020. Downloaded by Boston University on 8/21/2020 1:44:06 PM.

Nanoscale Accepted Manuscript

3.4 Binding Affinity to a Charged Peptide

As a simple exploration of how electrostatic properties dictate the binding between nanoparticles and biomolecules, we apply umbrella sampling to compute the potential of mean force profiles of nanoparticles interacting with a short, negatively charged peptide, Asp_8. The PMF profiles shown in Fig. 6 exhibit plateaus in the long-range, supporting the proper convergence of the results. The positions of the minimum in the PMFs are consistent with the locations of the ligand nitrogens expected based on the nanoparticle-nitrogen number densities (Fig. S3). The PMFs display significant differences in the binding affinity among nanoparticles functionalized with ligands differing in titration state and chemical nature. The PMFs of C4P65 and C4Q65 display a difference of ∼6 kcal/mol in binding affinity, highlighting the importance of hydrogen bonding between the carboxylate and primary amine groups. However, with the more realistic protonation pattern in C4P32-C4N33, the difference in the binding affinity between the primary amines and quaternary amines decreases to within ∼2 kcal/mol, highlighting the importance of assigning the proper titration state to ligands. The particle with mixed primary amines of different lengths, C8P32-C4P33, exhibits the highest binding affinity to Asp_8; previous MC/MD simulations[55] suggest that a majority of the amines in this case remains protonated at neutral pH because they are able to avoid each other spatially unlike the case of C4P65, which contains amines of equal alkyl chain length.

An intriguing observation concerns the difference between C4P32-C4N33 and C4P32-C4C33; although the latter features hydrophobic rather than polar (neutral amine) groups, the particle actually exhibits a stronger binding free energy to Asp_8 by a significant (∼2 kcal/mol) amount. This trend is consistent with the higher interfacial potential of C4P32-C4C33 than C4P32-C4N33 (Table 4), despite the similar apparent charges of these particles (Table 2), again pointing to the importance of interfacial solvent distributions modulated by the surface ligands. As shown in Fig. 7a, the hydration of charged amines in these particles are similar and the hydration of C4C is substantially lower than C4N, leading to an overall reduced level of interfacial hydration of the C4P32-C4C33 particle. Moreover, the angular

View Article Online
DOI: 10.1039/D0NR03792C

Published on 21 August 2020. Downloaded by Boston University on 8/21/2020 1:44:06 PM.

Nanoscale Accepted Manuscript

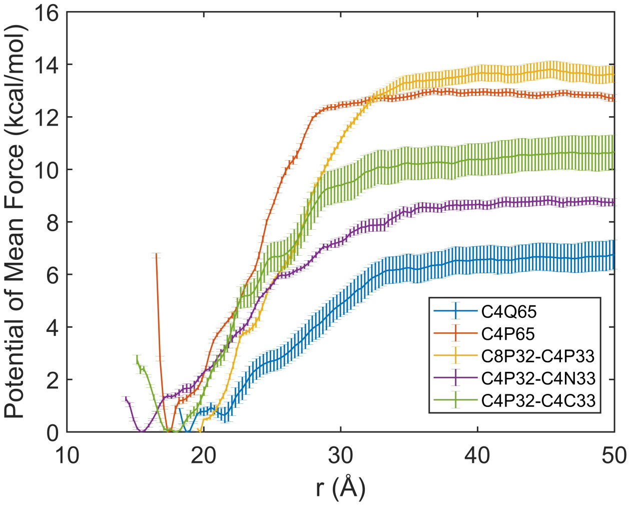

(a)

Figure 6: Potential of mean force of an Asp_8 peptide binding to different nanoparticles in 150 mM NaCl solution from umbrella sampling simulations. The r as shown is defined as the distance between the nanoparticle center and the center of mass of the peptide. For results for Asp_8 with 50% sidechains protonated, see Sect. 3 of the **Supporting Information**.

distributions of water molecules at the NP surface also differ when hydrophobic groups are introduced (Fig. 7b).

We note that the minima of the PMF profiles are all within the location of the slipping planes identified based on the fitting of chloride RDF to the Debye-Hückel expression. This suggests that the bound peptide is likely to displace counterions originally bound to the nanoparticle (see Fig. 8). Indeed, as shown in Table 5, the numbers of counterions within the slipping plane before and after peptide binding differ by a notable degree. Therefore, upon the binding of a small peptide, on the order of 3-8 counterions (mainly Cl^- ions) are released into the bulk solution, which is expected to also contribute to the binding free energy through an entropic term.[88,89]

View Article Online
DOI: 10.1039/D0NR03792C

Published on 21 August 2020. Downloaded by Boston University on 8/21/2020 1:44:06 PM.

Nanoscale Accepted Manuscript

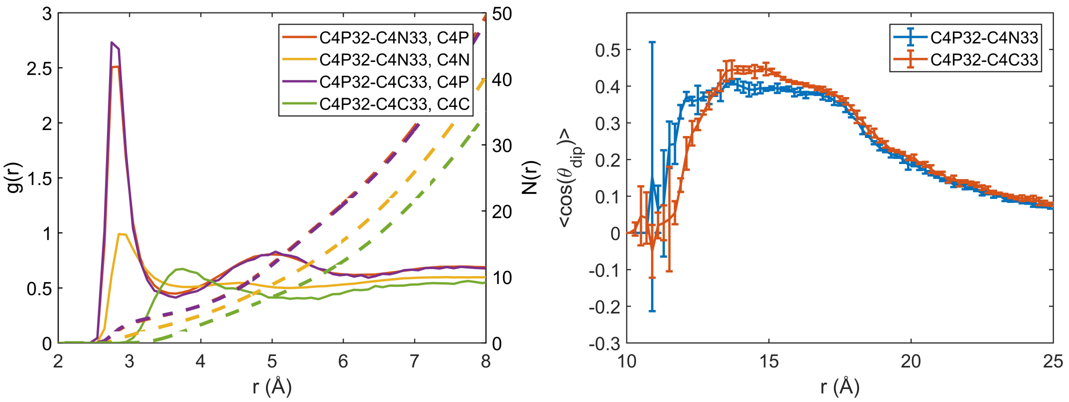

(a) (b)

Figure 7: Water distribution at the surface of C4P32-C4N33 and C4P32-C4C33 nanoparticles from MD simulations with 150 mM NaCl. (a) Radial distribution function of water oxygen with respect to the heavy atoms of ligand head groups (Nitrogen for C4P and C4N, Carbon for C4C). (b) Angular distribution (the cosine values) of the water dipole with respect to the nanoparticle surface normal.

Table 5: Counter ions (Na^+, Cl^-) released from the gold nanoparticle and the Asp_8 peptide upon binding[a].

Nanoparticle	Cl^- release	Na^+ release
C4Q65	8.1 ± 0.4	0.2 ± 0.4
C4P65	7.8 ± 0.1	1.3 ± 0.8
C8P32-C4P33	8.6 ± 2.1	0.2 ± 0.8
C4P32-C4N33	3.3 ± 0.7	1.9 ± 1.2
C4P32-C4C33	3.8 ± 0.8	1.4 ± 0.9

a. Ion release from the nanoparticle is estimated from the difference in the number of ions within the slipping plane between peptide-bound and -unbound cases taken from the corresponding windows of umbrella sampling simulations; the latter is presented in Table 2. For the ion release from the peptide, estimate is made based on the first peak of Na^+-carboxylate oxygen radial distribution function.

View Article Online
DOI: 10.1039/D0NR03792C

Published on 21 August 2020. Downloaded by Boston University on 8/21/2020 1:44:06 PM.

Nanoscale Accepted Manuscript

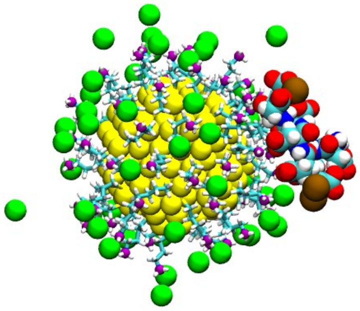

(a)

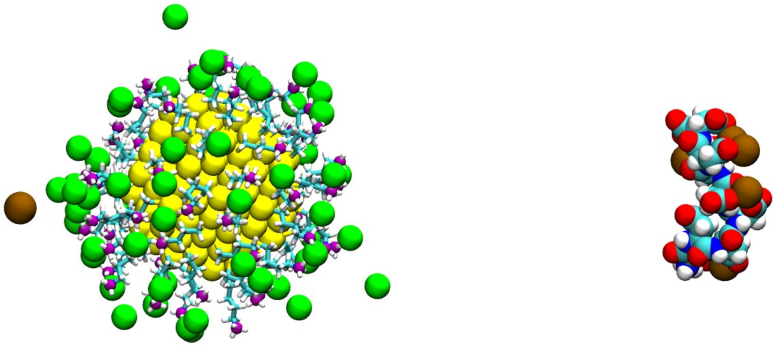

(b)

Figure 8: Snapshots from umbrella sampling simulations that illustrate the counterion distribution around the nanoparticle (C4P65) in the (a) peptide-bound and (b) unbound windows. Color coding: Au - yellow, C - cyan, Cl - green, Na - brown, N - blue, O - red, H - white; the head-group nitrogens of C4P ligands are shown in purple.

View Article Online
DOI: 10.1039/D0NR03792C
Published on 21 August 2020. Downloaded by Boston University on 8/21/2020 1:44:06 PM.
Nanoscale Accepted Manuscript

3.5 Discussion

The idea that highly charged surfaces are compensated by counterions has been appreciated for more than a century[90–92] and the degree of charge compensation has been theoretically or computationally studied using a broad range of models that included Poisson-Boltzmann,[25,51] integral equation theories,[47] classical density functional theories[24,93] and molecular simulations.[48] These pioneering theoretical treatments often employ highly simplified models for the surface and solvent and therefore do not capture effects due to the molecular nature of functionalized surfaces and solvent; similarly, experimental studies[94,95] also focused largely on homogeneous surfaces. Therefore, much remains to be learned concerning how *nanoscale* surface features impact interfacial charge distribution, solvation and binding. Indeed, detailed analysis of interfacial charge distribution with an atomistic level description of heterogeneous surfaces, solvent and ions only started to appear in the recent literature,[42,56,58,96] including the discussion of potential caveats in applying popular force field models.[78,97] On the experimental side, a quantitative analysis of interfacial charge distribution and solvation[98–100] with molecular level of detail has become feasible with sophisticated non-linear spectroscopies.[29,101] Therefore, subtle but potentially important features of interfacial charge and solvation distributions and their impact on binding warrant systematic analysis.

3.5.1 Difference between apparent charge and bare charge of nanoparticles depends on ligand properties and counterions

Significant charge compensation by counterions is observed for all the charged nanoparticles studied here, such that the apparent charge is in the same range even for particles whose bare charges (densities) differ by a factor of two (e.g., C4P65 vs. C4P32-C4N33). This large degree of charge compensation is observed at not only physiological salt concentration (150 mM NaCl) but also the relatively low salt concentration of 50 mM; the precise magnitude of compensation is, as expected, larger at the higher salt concentration, leading to lower apparent charges. The charged nanoparticles studied here have a bare charge of either 32

View Article Online
DOI: 10.1039/D0NR03792C

Published on 21 August 2020. Downloaded by Boston University on 8/21/2020 1:44:06 PM.

Nanoscale Accepted Manuscript

or 65, which correspond to a surface charge density of ∼0.18 and 0.37 C/m^2, respectively (assuming an effective radius of 1.5 nm); the apparent charge is ∼20 (10) at 50 mM (150 mM), which corresponds to a surface charge density of ∼0.11 (0.06) C/m^2. These findings are qualitatively consistent with the Manning condensation theory,[51,52] which predicts that ion condensation sets in at a surface charge density of $\frac{e(1+\kappa a)ln(\kappa l_B)}{2\pi l_B a}$, beyond which the apparent charge density is largely independent of the bare charge density; the critical surface density in the Manning theory is ∼0.03 C/m^2 at 50 mM, which is much lower than the saturation value of ∼0.1 C/m^2 observed in our simulation. Along this line, we note that recent vibrational sum-frequency-generation (VSFG) study[101] observed that interfacial water orientation at charged lipid surfaces saturates beyond the bare charge density of 0.1 C/m^2, presumably because the apparent surface charge density becomes independent of bare surface charge density due to counterion condensation.

The computed apparent charge from our microscopic simulations differ significantly from the prediction of the Manning theory at both salt concentrations studied. At 150 mM NaCl, for example, the computed Q_{app} varies between 10 and 17 e, while the Manning prediction is 1.2 e; the difference is very large and can not be explained by uncertainty in the definition of the slipping plane location (i.e., the definition of the Stern layer). As noted above and further discussed below, the interfacial electrostatic potential computed from our microscopic simulations, nevertheless, agrees well with the Manning prediction. To reconcile the contrasting trends in apparent charge and interfacial potential, it is important to recognize that solvent is treated at the continuum level in the Manning theory, while current and previous MD simulations[55] clearly indicate that interfacial water molecules are highly oriented and thus contribute to the interfacial charge distribution (see, for example, Fig. S7), even when explicit charge transfer involving interfacial water[102,103] is not considered; the simulation and VSFG study of Bonn and co-workers[101] also supported that water is an important component of the Stern layer of charged lipid surfaces.

The current microscopic simulations also highlight that the molecular features of the

View Article Online

DOI: 10.1039/D0NR03792C

Published on 21 August 2020. Downloaded by Boston University on 8/21/2020 1:44:06 PM.

Nanoscale Accepted Manuscript

surface ligand can impact counterion correlation and thus the apparent charge. While the observation of lower counterion correlation with quaternary amines than with primary amines is not unexpected, the finding that ligand length heterogeneity (C8P32-C4P33) also has a considerable impact on apparent charge underscores the need to include molecular level details. Regarding the impact of force field, it is encouraging that results from CHARMM36 and the polarizable Drude model are largely consistent, suggesting that an explicit inclusion of electronic polarizability is not essential for monovalent counterions, even for charged surfaces with as high bare charge density as 0.37 C/m^2. Finally, we note that we have focused on a single pair of counterions (Na$^+$, Cl$^-$), while several studies[29,56] have pointed to ion-specific effects on apparent surface charges of nanoparticles, a topic well-appreciated in biophysics[96] that again requires a molecular description of the interface. For example, with softer counterions (e.g., SCN$^-$) that favor pairing with the softer quaternary amines,[104] the trends in apparent charge and ζ potential can be very different from those observed here with chloride ions.

3.5.2 Interfacial water makes major contributions to interfacial potential and binding

As already alluded to above and in numerous previous discussions,[56,98,101,105] interfacial water molecules behave distinctly from bulk water and thus contribute significantly to the properties of interfaces. In the current study, two features stand out in particular to underscore the importance of interfacial hydration. First, while the apparent charge (Q_{app}) depends mostly on counterion correlation, the interfacial potential also depends on local hydration and thus exhibits more sensitivity to the chemical nature of the ligand. For example, at 50 mM NaCl, C4P65, C4P32-C4N33 and C4P32-C4C33 have similar $Q_{app}(r_{slip}) \sim 15e$, yet the interfacial potential for C4P32-C4C33, which contains 50% hydrophobic ligands, is considerably *higher* than the former two particles that have only polar/charged ligands. Second, along the same line, the binding affinity to an anionic peptide, Asp$_8$, is considerably *higher*

View Article Online
DOI: 10.1039/D0NR03792C

Published on 21 August 2020. Downloaded by Boston University on 8/21/2020 1:44:06 PM.

Nanoscale Accepted Manuscript

for C4P32-C4C33 compared to C4P32-C4P33. These observations highlight that introducing hydrophobic groups to nanoparticle surface can modulate the electrostatic properties such as interfacial potential and binding affinity to charged molecules. Since the counterions (Na^+, Cl^-) used in our study are in the middle of the Hofmeister series,[96] they do not exhibit significant binding to hydrophobic groups and therefore the current observations are likely driven by the different level of local hydration and water orientations[106,107] (Fig. 7); this is supported by the similar $Q_{app}(r_{slip})$ values observed for these particles. We note that the notion of enhanced electrostatic interactions near hydrophobic surfaces due to modified dielectric properties of interfacial water has been discussed in recent literature.[108–110]

3.5.3 Mobility and ζ potential do not always characterize apparent charge or binding affinity

An important motivation for the current work is to understand to what degree electrophoretic mobility and ζ potential reflect the bare or apparent charge of nanoparticles. While there is uncertainty in precisely defining the slipping plane at the molecular level, and that non-equilibrium molecular dynamics simulations have to use a fairly high electric field compared to experiments, several trends emerge from our analysis of a series of related nanoparticles. Foremost, even at a moderate salt concentration of 50 mM, the apparent surface charge density saturates to 0.1 C/m^2 ($\sim 20\ e$ on the surface of a 1.5 nm-radius nanoparticle) due to counterion condensation; as a result, the interfacial potential ζ_{ESP} does not correlate with the bare charge density. We note that the bare surface charge density of nanoparticles can well exceed the threshold of 0.1 C/m^2. For example, the recent study of Meng et al.[62] found that the ligand density for (16-mercaptohexadecyl) trimethylammonium bromide (MTAB) on the surface of gold nanoparticle/nanorod is in the range of $\sim$2 molecules/nm^2 for low-curvature surfaces to $\sim$6 molecules/nm^2 for high-curvature surfaces; these correspond to a bare charge density of 0.3 and 1.0 C/m^2, respectively. Therefore, for these nanoparticles, ion condensation is important even at moderate salt concentration (e.g., 50 mM) and ζ potential

View Article Online
DOI: 10.1039/D0NR03792C

Published on 21 August 2020. Downloaded by Boston University on 8/21/2020 1:44:06 PM.

Nanoscale Accepted Manuscript

does not correlate at all with the bare charge density.

Comparison of ζ_{ESP} and $Q_{app}(r_{slip})$ for different salt concentrations (see Tables 2, 4) suggests that ζ potential does generally correlate with the magnitude of apparent surface charge (density); reducing the salt concentration from 150 mM to 50 mM, the $Q_{app}(r_{slip})$ values increase by a factor of 1.2-1.5, and the ζ_{ESP} values also increase by a factor of $\sim$3. On the other hand, comparing ζ_{ESP} for different particles at the same salt concentration, we see a range of behaviors. On one hand, quaternary amine ligands lead to a higher apparent charge density than primary amine ligands due to a lower degree of Cl^- correlation; correspondingly, the ζ_{ESP} values are higher for quaternary amine decorated particles. On the other hand, while the apparent charge density of C4P33-C4C33 is similar to that of C4P33-C4N33, the ζ_{ESP} of the former is considerably higher (30.9±1.3 vs. 24.0±1.4 mV), highlighting again the importance of interfacial hydration. In the **Supporting Information**, we discuss some preliminary experimental measurements of ζ potential for a series of nanodiamond particles that qualitatively support these computational findings.

An intriguing observation from the current work is that the ζ potential estimated from mobility calculations and the Smoluchowski theory (Eq. 2) differs substantially from the microscopic electrostatic potential calculations. As shown in Table 4, the difference between ζ_{mob} and ζ_{ESP} is modest at the low salt (50 mM) condition but rather significant (a factor of $\sim$3) at the physiological salt concentration; the latter seems difficult to reconcile based only on the uncertainty in r_{slip}. Such discrepancies likely reflect the limitations of the Smoluchowski theory, which employed a bulk continuum description of the solvent for both viscosity and dielectric properties; numerous studies have indicated that these water properties near charged and non-polar surfaces are distinct from the bulk.[111,112] For example, the effective dielectric constant near charged surfaces can be significantly lower than the bulk value due to strongly orientated interfacial water,[56,113,114] thus using the bulk dielectric constant in Eq. 2 leads to underestimation of the ζ potential (although ζ_{mob} is *higher* than ζ_{ESP}). Also, the Smoluchowski model does not consider the thickness of the electrical double

View Article Online
DOI: 10.1039/D0NR03792C

Published on 21 August 2020. Downloaded by Boston University on 8/21/2020 1:44:06 PM.

Nanoscale Accepted Manuscript

layer or its polarization in the presence of the external field.[41] This is partially described through the Henry's function,[60] $H(\kappa a)$ in Eq. 2, which has a value between 1 and 3/2; the value is ∼1.06 for our case and thus a modest revision compared to the difference between ζ_{mob} and ζ_{ESP}. On the other hand, we note that the simulation has to employ a rather high electric field (10^5 higher than the typical experimentally applied value), which as shown in Fig. S11 can lead to an overestimation of drift velocity.

Another important observation from the current work is that mobility and ζ potentials are not reliable predictors for binding affinity of nanoparticles to charged molecules. First, binding interactions depend critically on the chemical details of the groups involved. For the cases explored here, primary amines interact more favorably with aspartate than do quaternary amines. Therefore, although C4Q65 has considerably higher interfacial potential than C4P65 or C4P33-C4N32, its binding affinity to Asp_8 is substantially lower. Second, the electric double layer is perturbed upon binding (Fig. 8, Table 5), thus the binding affinity in fact correlates with *bare charge density* even though the interfacial potential of the unbound particle correlates better with *apparent charge density* due to counterion binding. For example, both C4P65 and C8P32-C4P33 exhibit much higher binding affinities to Asp_8 than other nanoparticles although their ζ_{ESP} values are not among the highest ones.

3.5.4 Design rules for charged interactions at the nano/bio interface

While the systems explored in this study are relatively simple in molecular composition, the results highlight a number of design rules that can be employed to modulate electrostatic driven interactions at nano/bio interfaces. Foremost, it is essential to consider specific chemical interactions such as salt-bridge or hydrogen-bonding interactions between the binding partners; for example, employ primary amines to enhance interactions to acidic groups while choose quaternary amines for minimizing such interactions. Second, maximize the *bare charge density* rather than the *apparent charge density* since the electric double layer is likely perturbed upon binding. Along this line, it is important to recall that the bare charge den-

View Article Online
DOI: 10.1039/D0NR03792C

Published on 21 August 2020. Downloaded by Boston University on 8/21/2020 1:44:06 PM.

sity does not increase monotonically as a function of ligand density, when titratable groups are involved.[55] One possible strategy is to mix charged ligands of heterogeneous length and flexibility, which enable titratable groups to avoid each other and minimize electrostatic coupling. It is also possible to employ the MC/MD approach[55] to optimize the ligand density for the desirable charge density or charge capacity.[115] Third, it can be productive to decorate the surface with a fraction of hydrophobic groups, which can modulate the level and properties of interfacial hydration that in turn influence the strength of electrostatic interactions at the interface. Moreover, for the choice of charged ligands, it is valuable to bear in mind specific ion effects[104] for modulating the degree of counterion correlation in the specific solution environment of interest.

4 Conclusions

To modulate interactions between nanoparticles and (bio)molecules for applications, it is important to understand the physical and chemical factors that dictate such interactions. In this work, we target electrostatic interactions because many nanoparticles and biomolecules are highly charged. While electrostatic properties of charged surfaces, colloid particles and nanoparticles have been studied for more than a century, much remain to be learned about electrostatics at the nanoscale, for which deviations from predictions by mean-field and continuum theories are anticipated due to the importance of molecular scale features.

By comparing simulation results for a set of nanoparticles with different surface ligands, we are able to glean new insights into factors that dictate the interfacial electrostatic properties and interaction with charged biomolecules. Similar to predictions of mean-field models such as the Manning condensation theory, counterions are observed to screen the bare ligand charge to a significant degree even at a moderate salt concentration of 50 mM. With the surface ligand density typically measured in experiments (∼2-6 molecules/nm^2), condensation of counterions leads to the observation that the apparent charge density and ζ potential are

Nanoscale Accepted Manuscript

View Article Online
DOI: 10.1039/D0NR03792C

Published on 21 August 2020. Downloaded by Boston University on 8/21/2020 1:44:06 PM.

Nanoscale Accepted Manuscript

largely independent of the bare charge density; this result is not sensitive to the treatment of electronic polarization, likely because the counterions are monovalent in our study. The chemical nature of the charged ligand (e.g., primary vs. quaternary amines), however, can modulate the magnitude of counterion correlation and therefore the interfacial potential. Moreover, introducing a fraction of hydrophobic ligands modulates the interfacial solvent distribution and thus also perturbs the interfacial potential. These molecular features of the interface are not captured in well-established mean-field models; for example, the critical and saturated apparent charge densities from Manning theory are rather different from the results of our microscopic simulations.

While counterions contribute significantly to the electrostatic properties of nanoparticles, our simulations highlight that the electric double layer is perturbed upon binding interactions. As a result, it is the bare charge density rather than the apparent charge density that better correlates with binding affinity of the nanoparticle to a charged peptide; for this reason, carefully treating the titration behaviors of surface ligands is essential to an accurate evaluation of nano/bio binding interactions. Therefore, strategies that enhance bare surface charge, such as mixing ligands of heterogeneous length and flexibility, can be effective for enhancing interactions. In addition, modulation of interfacial solvation by introducing a fraction of hydrophobic ligands to the nanoparticle surface also provides further tunability. Along this line, we note that our study treated the ligands as randomly mixed at the surface, although it is possible that ligands of very different chemical natures can phase separate to form domains;[116–118] surface ligand distribution may also respond to the binding of biomolecules.[119] These fascinating aspects of nano/bio interfaces will be examined in future studies.

View Article Online
DOI: 10.1039/D0NR03792C

Published on 21 August 2020. Downloaded by Boston University on 8/21/2020 1:44:06 PM.

Nanoscale Accepted Manuscript

Acknowledgement

This work was supported by the National Science Foundation under the Center for Sustainable Nanotechnology, CHE-1503408. The CSN is part of the Centers for Chemical Innovation Program. Computational resources from the Extreme Science and Engineering Discovery Environment (XSEDE), which is supported by NSF grant number OCI-1053575, are greatly appreciated; part of the computational work was performed on the Shared Computing Cluster which is administered by Boston University's Research Computing Services (URL: www.bu.edu/tech/support/research/). D. Ray was supported by a Bose Fellowship during his visit to the Cui group at UW-Madison.

Supporting Information

Additional results for counterion distribution, ligand distribution, interfacial electrostatic potential, apparent charge profile, drift velocity simulations, and impact of the core structure are included. Also included are binding free energy simulation for Asp_8 with a different protonation pattern as well as experimental measurement of ζ potential for several nanodiamond particles functionalized with different ligands.

References

(1) Arico, A. S.; Bruce, P.; Scrosati, B.; Tarascon, J.-M.; Van Schalkwijk, W. *Materials For Sustainable Energy: A Collection of Peer-Reviewed Research and Review Articles from Nature Publishing Group*; World Scientific, 2011; pp 148–159.

(2) Khin, M. M.; Nair, A. S.; Babu, V. J.; Murugan, R.; Ramakrishna, S. A review on nanomaterials for environmental remediation. *Energy Environ. Sci.* **2012**, *5*, 8075–8109.

View Article Online
DOI: 10.1039/D0NR03792C

Published on 21 August 2020. Downloaded by Boston University on 8/21/2020 1:44:06 PM.

Nanoscale Accepted Manuscript

(3) Shannon, M. A.; Bohn, P. W.; Elimelech, M.; Georgiadis, J. G.; Marinas, B. J.; Mayes, A. M. *Nanoscience and technology: a collection of reviews from nature Journals*; World Scientific, 2010; pp 337–346.

(4) Huang, X.; El-Sayed, I. H.; Qian, W.; El-Sayed, M. A. Cancer cell imaging and photothermal therapy in the near-infrared region by using gold nanorods. *J. Am. Chem. Soc.* **2006**, *128*, 2115–2120.

(5) Gao, X.; Cui, Y.; Levenson, R. M.; Chung, L. W.; Nie, S. In vivo cancer targeting and imaging with semiconductor quantum dots. *Nature Biotechnol.* **2004**, *22*, 969.

(6) Langer, R.; Tirrell, D. A. Designing materials for biology and medicine. *Nature* **2004**, *428*, 487.

(7) Michalet, X.; Pinaud, F.; Bentolila, L.; Tsay, J.; Doose, S.; Li, J.; Sundaresan, G.; Wu, A.; Gambhir, S.; Weiss, S. Quantum dots for live cells, in vivo imaging, and diagnostics. *Science* **2005**, *307*, 538–544.

(8) Ferrari, M. Cancer nanotechnology: opportunities and challenges. *Nat. Rev. Cancer* **2005**, *5*, 161.

(9) Giljohann, D. A.; Seferos, D. S.; Daniel, W. L.; Massich, M. D.; Patel, P. C.; Mirkin, C. A. Gold nanoparticles for biology and medicine. *Angew. Chem. Int. Ed.* **2010**, *49*, 3280–3294.

(10) Jain, S.; Hirst, D.; O'sullivan, J. Gold nanoparticles as novel agents for cancer therapy. *Br. J. Radiol.* **2012**, *85*, 101–113.

(11) Lara, Y.; Nguyen, T.; Marilena, L.; Alexander, M. Toxicological considerations of clinically applicable nanoparticles. *Nano Today* **2011**, *6*, 585–607.

(12) Murphy, C. J.; Vartanian, A. M.; Geiger, F. M.; Hamers, R. J.; Pedersen, J.; Cui, Q.; Haynes, C. L.; Carlson, E. E.; Hernandez, R.; R. D. Klaper et al., Biological Responses

View Article Online
DOI: 10.1039/D0NR03792C

Published on 21 August 2020. Downloaded by Boston University on 8/21/2020 1:44:06 PM.

Nanoscale Accepted Manuscript

to Engineered Nanomaterials: Needs for the Next Decade. *ACS Central Sci.* **2015**, *1*, 117–123.

(13) Hamers, R. J. Nanomaterials and Global Sustainability. *Acc. Chem. Res.* **2017**, *50*, 633–637.

(14) Cui, Q.; Hernandez, R.; Mason, S. E.; Frauenheim, T.; Pedersen, J. A.; Geiger, F. Sustainable nanotechnology: opportunities and challenges for theoretical/computational studies. *J. Phys. Chem. B* **2016**, *120*, 7297–7306.

(15) Hochella Jr., M. F.; Mogk, D. W.; Ranville, J.; Allen, I. C.; Luther, G. W.; Matt, L. C.; McGrail, B. P.; Murayama, M.; Qafoku, N. P.; Rosso, K. M. et al., Natural, Incidental, and Engineered Nanomaterials and Their Impacts on the Earth System. *Science* **2019**, *363*, eaau8299.

(16) Albanese, A.; Tang, P. S.; Chan, W. C. W. The Effect of Nanoparticle Size, Shape, and Surface Chemistry on Biological Systems. *Annu. Rev. Biomed. Engn.* **2012**, *14*, 1–16.

(17) Monopoli, M. P.; Aberg, C.; Salvati, A.; Dawson, K. A. Biomolecular Coronas Provide the Biological Identity of Nanosized Materials. *Nat. Nanotech.* **2012**, *7*, 779–786.

(18) Olenick, L. L.; Troiano, J. M.; Vartanian, A.; Melby, E. S.; Mensch, A. C.; Zhang, L.; Hong, J.; Mesele, O.; Qiu, T.; Bozich, J.; Lohse, S.; Zhang, X.; Kuech, T. R.; Millevolte, A.; Gunsolus, I.; McGeachy, A. C.; Doğangün, M.; Li, T.; Hu, D.; Walter, S. R.; Mohaimani, A.; Schmoldt, A.; Torelli, M. D.; Hurley, K. R.; Dalluge, J.; Chong, G.; Feng, Z. V.; Haynes, C. L.; Hamers, R. J.; Pedersen, J. A.; Cui, Q.; Hernandez, R.; Klaper, R.; Orr, G.; Murphy, C. J.; Geiger, F. M. Lipid Corona Formation from Nanoparticle Interactions with Bilayers. *Chem* **2018**, *4*, 2709–2723.

(19) Dominguez-Medina, S.; Kisley, L.; Tauzin, L. J.; Hoggard, A.; Shuang, B.; Indrasekara, A. S. D. S.; Chen, S. S.; Wang, L. Y.; Liopo, A.; Zubarev, E. R.; Lan-

View Article Online
DOI: 10.1039/D0NR03792C

Published on 21 August 2020. Downloaded by Boston University on 8/21/2020 1:44:06 PM.

des, C. F.; Link, S. Adsorption and Unfolding of a Single Protein Triggers Nanoparticle Aggregation. *ACS Nano* **2016**, *10*, 2103–2112.

(20) Attwood, S. J.; Kershaw, R.; Uddin, S.; Bishop, S. M.; Welland, M. E. Understanding how charge and hydrophobicity influence globular protein adsorption to alkanethiol and material surfaces. *J. Mater. Chem. B* **2019**, *7*, 2349.

(21) Payne, C. K. A protein corona primer for physical chemists. *J. Chem. Phys.* **2019**, *151*, 130901.

(22) Nel, A. E.; Madler, L.; Velegol, D.; Xia, T.; Hoek, E. M. V.; Somasundaran, P.; Klaessig, F.; Castranova, V.; Thompson, M. Understanding biophysicochemical interactions at the nano-bio interface. *Nat. Mater.* **2009**, *8*, 543–557.

(23) Petros, R. A.; DeSimone, J. M. Strategies in the design of nanoparticles for therapeutic applications. *Nat. Rev. Drug Discov.* **2010**, *9*, 615–627.

(24) Walker, D. A.; Kowalczyk, B.; de la Cruz, M. O.; Grzybowski, B. A. Electrostatics at the nanoscale. *Nanoscale* **2011**, *3*, 1316–1344.

(25) Barrat, J.-L.; Hansen, J.-P. *Basic concepts for simple and complex liquids*; Cambridge University Press, 2003.

(26) Netz, R. R.; Andelman, D. Neutral and charged polymers at interfaces. *Phys. Rep.* **2003**, *380*, 1–95.

(27) Dobrynin, A. V.; Rubinstein, M. Theory of polyelectrolytes in solutions and at surfaces. *Prog. Poly. Sci.* **2005**, *30*, 1049–1118.

(28) You, C. C.; De, M.; Han, G.; Rotello, V. M. Tunable Inhibition and Denaturation of r-Chymotrypsin with Amino Acid-Functionalized Gold Nanoparticles. *J. Am. Chem. Soc.* **2005**, *127*, 12873–12881.

Nanoscale Accepted Manuscript

View Article Online
DOI: 10.1039/D0NR03792C

Published on 21 August 2020. Downloaded by Boston University on 8/21/2020 1:44:06 PM.

(29) Zdrali, E.; Okur, H. I.; Roke, S. Specific Ion Effects at the Interface of Nanometer-Sized Droplets in Water: Structure and Stability. *J. Phys. Chem. C* **2019**, *123*, 16621–16630.

(30) Troiano, J. M.; Olenick, L. L.; Kuech, T. R.; Melby, E. S.; Hu, D.; Lohse, S. E.; Mensch, A. C.; Dogangun, M.; Vartanian, A. M.; M. D. Torelli et al., Direct Probes of 4-nm Diameter Gold Nanoparticles Interacting with Supported Lipid Bilayers. *J. Phys. Chem. C* **2015**, *119*, 534.

(31) Bozich, J. S.; Lohse, S. E.; Torelli, M. D.; Murphy, C. J.; Hamers, R. J.; Klaper, R. D. Surface chemistry, charge and ligand type impact the toxicity of gold nanoparticles to Daphnia magna. *Environ. Sci. Nano* **2014**, *13*, 260–270.

(32) Dominguez, G. A.; Lohse, S. E.; Torelli, M. D.; Murphy, C. J.; Hamers, R. J.; Orr, G.; Klaper, R. D. Effects of Charge and Surface Ligand Properties of Nanoparticles on Oxidative Stress and Gene Expression within the Gut of Daphnia Magna. *Aquatic Toxicol.* **2015**, *162*, 19.

(33) Pmobo Garcia, K.; Zarschler, K.; Barbaro, L.; Barreto, J. A.; O'Malley, W.; Spiccia, L.; Stephan, H.; Graham, B. Zwitterionic-coated "stealth" nanoparticles for biomedical applications: recent advances in countering biomolecular corona formation and uptake by the mononuclear phagocyte system. *Small* **2014**, *10*, 2516–2529.

(34) Zhang, X.; Pandiakumar, A. K.; Hamers, R. J.; Murphy, C. J. Quantification of Lipid Corona Formation on Colloidal Nanoparticles from Lipid Vesicles. *Anal. Chem.* **2018**, *90*, 14387–14394.

(35) Melby, E. S.; Lohse, S. E.; Park, J. E.; Vartanian, A. M.; Putans, R. A.; Abbott, H. B.; Hamers, R. J.; Murphy, C. J.; Pedersen, J. A. Cascading Effects of Nanoparticle Coatings: Surface Functionalization Dictates the Assemblage of Complexed Proteins and Subsequent Interaction with Model Cell Membranes. *ACS Nano* **2017**, *11*, 5489–5499.

Nanoscale Accepted Manuscript

View Article Online
DOI: 10.1039/D0NR03792C

(36) Melby, E. S.; Allen, C.; Foreman-Ortiz, I. U.; Caudill, E. R.; Kuech, T. R.; Vartanian, A. M.; Zhang, X.; Murphy, C. J.; Hernandez, R.; Pedersen, J. A. Peripheral Membrane Proteins Facilitate Nanoparticle Binding at Lipid Bilayer Interfaces. *Langmuir* **2018**, *34*, 10793–10805.

(37) Tollefson, E. J.; Allen, C. R.; Chong, G.; Zhang, X.; Rozanov, N. D.; Bautista, A.; Cerda, J. J.; Pedersen, J. A.; Murphy, C. J.; Carlson, E. E.; Hernandez, R. Preferential binding of cytochrome c to anionic ligand-coated gold nanoparticles: A complementary computational and experimental approach. *ACS Nano* **2019**, *13*, 6856–6866.

(38) Delgado, Á. V.; González-Caballero, F.; Hunter, R.; Koopal, L.; Lyklema, J. Measurement and interpretation of electrokinetic phenomena. *J. Colloid Interface Sci.* **2007**, *309*, 194–224.

(39) Doane, T. L.; Chuang, C.-H.; Hill, R. J.; Burda, C. Nanoparticle ζ-potentials. *Acc. Chem. Res.* **2011**, *45*, 317–326.

(40) Hunter, R. J. *Zeta potential in colloid science: principles and applications*; Academic press, 2013; Vol. 2.

(41) Lowry, G. V.; Hill, R. J.; Harper, S.; Rawle, A. F.; Hendren, C. O.; Klaessig, F.; Nobbmann, U.; Sayre, P.; Rumble, J. Guidance to improve the scientific value of zeta-potential measurements in nanoEHS. *Environ. Sci-Nano* **2016**, *3*, 953–965.

(42) Predota, M.; Machesky, M. L.; Wesolowski, D. J. Molecular origins of the Zeta potential. *Langmuir* **2016**, *32*, 10189–10198.

(43) Huang, Q. R.; Dubin, P. L.; Moorefield, C. N.; Newkome, G. R. Counterion Binding on Charged Spheres: Effect of pH and Ionic Strength on the Mobility of Carboxyl-Terminated Dendrimers. *J. Phys. Chem. B* **2000**, *104*, 898–904.

Published on 21 August 2020. Downloaded by Boston University on 8/21/2020 1:44:06 PM.

Nanoscale Accepted Manuscript

View Article Online
DOI: 10.1039/D0NR03792C

Published on 21 August 2020. Downloaded by Boston University on 8/21/2020 1:44:06 PM.

Nanoscale Accepted Manuscript

(44) von Smoluchowski, M. Contribution à la théorie de l'endosmose électrique et de quelques phénomènes corrélatifs. *Bull. Akad. Sci. Cracovie.* **1903**, *8*, 182–200.

(45) O'Brien, R. W.; White, L. R. Electrophoretic Mobility of a Spherical Colloidal Particle. *J. Chem. Soc. Faraday Trans. 2* **1978**, *74*, 1607–1626.

(46) Batista, C. A. S.; Larson, R. G.; Kotov, N. A. Nonadditivity of Nanoparticle Interactions. *Science* **2015**, *350*, 1242477.

(47) Gonzalez-Tovar, E.; Lozada-Cassou, M. The spherical double layer: A hypernetted chain mean spherical approximation calculation for a model spherical colloid particle. *J. Phys. Chem.* **1989**, *93*, 3761–3768.

(48) Degreve, L.; Lozada-Cassou, M.; Sanchez, E.; Gonzalez-Tovar, E. Monte Carlo simulation for a symmetrical electrolyte next to a charged spherical colloid particle. *J. Chem. Phys.* **1993**, *98*, 8905–8909.

(49) Manning, G. S. Limiting laws and counterion condensation in polyelectrolyte solutions I. Colligative properties. *J. Chem. Phys.* **1969**, *51*, 924–933.

(50) Manning, G. S. Electrostatic free energies of spheres, cylinders, and planes in counterion condensation theory with some applications. *Macromolecules* **2007**, *40*, 8071–8081.

(51) Manning, G. S. Counterion condensation on charged spheres, cylinders, and planes. *J. Phys. Chem. B* **2007**, *111*, 8554–8559, 6th International Symposium on Polyelectrolytes, Dresden, GERMANY, SEP, 2006.

(52) Manning, G. S. The interaction between a charged wall and its counterions: A condensation theory. *J. Phys. Chem. B* **2010**, *114*, 5435–5440.

(53) Ullmann, G. M. Relations between Protonation Constants and Titration Curves in Polyprotic Acids: A Critical View. *J. Phys. Chem. B* **2003**, *107*, 1263–1271.

View Article Online
DOI: 10.1039/D0NR03792C

(54) Konek, C. T.; Musorrafiti, M. J.; Al-Abadleh, H. A.; Bertin, P. A.; Nguyen, S. T.; Geiger, F. M. Interfacial Acidities, Charge Densities, Potentials, and Energies of Carboxylic Acid-Functionalized Silica/Water Interfaces Determined by Second Harmonic Generation. *J. Am. Chem. Soc.* **2004**, *126*, 11754–11755.

(55) Hong, J.; Hamers, R. J.; Pedersen, J. A.; Cui, Q. A hybrid molecular dynamics/multiconformer continuum electrostatics (MD/MCCE) approach for the determination of surface charge of nanomaterials. *J. Phys. Chem. C* **2017**, *121*, 3584–3596.

(56) Bonthuis, D. J.; Netz, R. R. Beyond the continuum: How molecular solvent structure affects electrostatics and hydrodynamics at solid–electrolyte interfaces. *J. Phys. Chem., B* **2013**, *117*, 11397–11413.

(57) Wernersson, E.; Heyda, J.; Kubickova, A.; Krizek, T.; Coufal, P.; Jungwirth, P. Counterion condensation in short cationic peptides: Limiting mobilities beyond the Onsager–Fuoss theory. *Electrophoresis* **2012**, *33*, 981–989.

(58) Ge, Z.; Wang, Y. Estimation of Nanodiamond Surface Charge Density from Zeta Potential and Molecular Dynamics Simulations. *J. Phys. Chem. B* **2016**, *121*, 3394–3402.

(59) Zhang, Y.; Fry, C. G.; Pedersen, J. A.; Hamers, R. J. Dynamics and morphology of nanoparticle-linked polymers elucidated by nuclear magnetic resonance. *Anal. Chem.* **2017**, *89*, 12399–12407.

(60) Henry, D. The cataphoresis of suspended particles. Part I.—The equation of cataphoresis. *Proc. Royal Soc. A* **1931**, *133*, 106–129.

(61) Russel, W. B.; Saville, D. A.; Schowalter, W. R. *Colloidal Dispersions*; Cambridge University Press: New York, 1989.

Published on 21 August 2020. Downloaded by Boston University on 8/21/2020 1:44:06 PM.

Nanoscale Accepted Manuscript

View Article Online
DOI: 10.1039/D0NR03792C

Published on 21 August 2020. Downloaded by Boston University on 8/21/2020 1:44:06 PM.

(62) Wu, M.; Vartanian, A. M.; Chong, G.; Pandiakumar, A. K.; Hamers, R. J.; Hernandez, R.; Murphy, C. J. Solution NMR Analysis of Ligand Environment in Quaternary Ammonium-Terminated Self-Assembled Monolayers on Gold Nanoparticles: The Effect of Surface Curvature and Ligand Structure. *J. Am. Chem. Soc.* **2019**, *141*, 4316–4327.

(63) Sakthivel, N. A.; Theivendran, S.; Ganeshraj, V.; Oliver, A. G.; Dass, A. Crystal Structure of Faradaurate-279: $Au_{279}(SPh\text{-}tBu)_{84}$ Plasmonic Nanocrystal Molecules. *J. Am. Chem. Soc.* **2017**, *139*, 15450–15459.

(64) Heikkila, E.; Martinez-Seara, H.; Gurtovenko, A. A.; Vattulainen, I.; Akola, J. Atomistic simulations of anionic Au-144(SR)(60) nanoparticles interacting with asymmetric model lipid membranes. *Biochim. Biophys. Acta-Biomembranes* **2014**, *1838*, 2852–2860.

(65) Heikkilä, E.; Gurtovenko, A. A.; Martinez-Seara, H.; Häkkinen, H.; Vattulainen, I.; Akola, J. Atomistic Simulations of Functional $Au_{144}(SR)_{60}$ Gold Nanoparticles in Aqueous Environment. *J. Phys. Chem. C* **2012**, *116*, 9805–9815.

(66) Schmit, J. D.; Kariyawasam, N. L.; Needham, V.; Smith, P. E. SLTCAP: A simple method for calculating the number of ions needed for MD simulation. *J. Chem. Theory Comput.* **2018**, *14*, 1823–1827.

(67) Huang, J.; A. D. MacKerell Jr., CHARMM36 All-atom Additive Protein Force Field: Validation Based on Comparison to NMR Data. *J. Comput. Chem.* **2013**, *34*, 2135–2145.

(68) MacKerell, A. D.; Bashford, D.; Bellott, M.; Dunbrack, R. L.; Evanseck, J. D.; Field, M. J.; Fischer, S.; Gao, J.; Guo, H.; S. Ha et al., All-Atom Empirical Potential for Molecular Modeling and Dynamics Studies of Proteins. *J. Phys. Chem. B* **1998**, *102*, 3586–3616.

Nanoscale Accepted Manuscript

View Article Online
DOI: 10.1039/D0NR03792C

Published on 21 August 2020. Downloaded by Boston University on 8/21/2020 1:44:06 PM.

Nanoscale Accepted Manuscript

(69) Jorgensen, W. L.; Chandrasekhar, J.; Madura, J. D.; Impey, R. W.; Klein, M. L. Comparison of simple potential functions for simulating liquid water. *The Journal of chemical physics* **1983**, *79*, 926–935.

(70) Venable, R. M.; Luo, Y.; Gawrisch, K.; Roux, B.; Pastor, R. W. Simulations of anionic lipid membranes: development of interaction-specific ion parameters and validation using NMR data. *J. Phys. Chem. B* **2013**, *117*, 10183–10192.

(71) Heinz, H.; Lin, T.-J.; Kishore Mishra, R.; Emami, F. S. Thermodynamically consistent force fields for the assembly of inorganic, organic, and biological nanostructures: the INTERFACE force field. *Langmuir* **2013**, *29*, 1754–1765.

(72) Liang, D. Y.; Hong, J. W.; Dong, F.; Bennett, J. W.; Mason, S. E.; Hamers, R. J.; Cui, Q. Analysis of Conformational Properties of Amine Ligands at the Gold/Water Interface with QM, MM and QM/MM simulations. *Phys. Chem. Chem. Phys.* **2018**, *20*, 3349–3362.

(73) Phillips, J. C.; Braun, R.; Wang, W.; Gumbart, J.; Tajkhorshid, E.; Villa, E.; Chipot, C.; Skeel, R. D.; Kale, L.; Schulten, K. Scalable molecular dynamics with NAMD. *J. Comput. Chem.* **2005**, *26*, 1781–1802.

(74) Darden, T.; York, D.; Pedersen, L. Particle mesh Ewald: An N log (N) method for Ewald sums in large systems. *J. Chem. Phys.* **1993**, *98*, 10089–10092.

(75) Ryckaert, J.-P.; Ciccotti, G.; Berendsen, H. J. Numerical integration of the cartesian equations of motion of a system with constraints: molecular dynamics of n-alkanes. *J. Comput. Phys.* **1977**, *23*, 327–341.

(76) Brünger, A. T. *X-PLOR: version 3.1: a system for x-ray crystallography and NMR*; Yale University Press, 1992.

View Article Online
DOI: 10.1039/D0NR03792C

Published on 21 August 2020. Downloaded by Boston University on 8/21/2020 1:44:06 PM.

Nanoscale Accepted Manuscript

(77) Feller, S. E.; Zhang, Y.; Pastor, R. W.; Brooks, B. R. Constant pressure molecular dynamics simulation: the Langevin piston method. *J. Chem. Phys.* **1995**, *103*, 4613–4621.

(78) Duboue-Dijon, E.; Delcroix, P.; Martinez-Seara, H.; Hladilkova, J.; Coufal, P.; Krizek, T.; Jungwirth, P. Binding of Divalent Cations to Insulin: Capillary Electrophoresis and Molecular Simulations. *J. Phys. Chem. B* **2018**, *122*, 5640–5648.

(79) Lamoureux, G.; Harder, E.; Vorobyov, I. V.; Roux, B.; MacKerell Jr, A. D. A polarizable model of water for molecular dynamics simulations of biomolecules. *Chem. Phys. Lett.* **2006**, *418*, 245–249.

(80) Yu, H.; Whitfield, T. W.; Harder, E.; Lamoureux, G.; Vorobyov, I.; Anisimov, V. M.; MacKerell Jr, A. D.; Roux, B. Simulating monovalent and divalent ions in aqueous solution using a Drude polarizable force field. *J. Chem. Theory Comput.* **2010**, *6*, 774–786.

(81) Lopes, P. E.; Huang, J.; Shim, J.; Luo, Y.; Li, H.; Roux, B.; MacKerell Jr, A. D. Polarizable force field for peptides and proteins based on the classical drude oscillator. *J. Chem. Theory Comput.* **2013**, *9*, 5430–5449.

(82) Jo, S.; Kim, T.; Iyer, V. G.; Im, W. CHARMM-GUI: a web-based graphical user interface for CHARMM. *J. Comput. Chem.* **2008**, *29*, 1859–1865.

(83) Yeh, I.-C.; Hummer, G. Diffusion and electrophoretic mobility of single-stranded RNA from molecular dynamics simulations. *Biophys. J* **2004**, *86*, 681–689.

(84) Grossfield, A. WHAM: the weighted histogram analysis method, version 2.0. 9. *Available at membrane. urmc. rochester. edu/content/wham. Accessed November* **2013**,

(85) Allen, M. P.; Tildesley, D. J. *Computer Simulation of Liquids, 2nd Ed.*; Oxford University Press: London, 2017.

View Article Online
DOI: 10.1039/D0NR03792C

Published on 21 August 2020. Downloaded by Boston University on 8/21/2020 1:44:06 PM.

Nanoscale Accepted Manuscript

(86) Jackson, J. D. *Classical Electrodynamics*; John Wiley & Sons: New York, 1975.

(87) Braun, D.; Boresch, S.; Steinhauser, O. Transport and dielectric properties of water and the influence of coarse-graining: Comparing BMW, SPC/E, and TIP3P models. *J. Chem. Phys.* **2014**, *140*, 064107.

(88) Vivcharuk, V.; Kaznessis, Y. Free Energy Profile of the Interaction between a Monomer or a Dimer of Protegrin-1 in a Specific Binding Orientation and a Model Lipid Bilayer. *J. Phys. Chem. B* **2010**, *114*, 2790–2797.

(89) Singh, A. N.; Yethiraj, A. Driving Force for the Complexation of Charged Polypeptides. *J. Phys. Chem. B* **2020**, *124*, 1285–1292.

(90) Gouy, G. *Compt. Rend.* **1910**, *149*, 654.

(91) Chapman, D. L. *Philos. Mag.* **1913**, *25*, 475.

(92) Stern, O. *Z. Elektrochem.* **1924**, *30*, 508.

(93) Hansen, J.-P.; McDonald, I. R. *Theory of Simple Liquids*; Academic Press: London, 2006.

(94) Lyklema, J. *Fundamentals of Interface and Colloid Science*; Academic Press: London, 1991.

(95) Israelachvili, J. N. *Intermolecular and Surface Forces, 3rd Ed.*; Academic Press: London, 2015.

(96) Okur, H. I.; Hladilkova, J.; Rembert, K. B.; Cho, Y.; Heyda, J.; Dzubiella, J.; Cremer, P. S.; Jungwirth, P. Beyond the Hofmeister Series: Ion-Specific Effects on Proteins and Their Biological Functions. *J. Phys. Chem. B* **2017**, *121*, 1997–2014.

View Article Online
DOI: 10.1039/D0NR03792C

Published on 21 August 2020. Downloaded by Boston University on 8/21/2020 1:44:06 PM.

Nanoscale Accepted Manuscript

(97) Walsh, T. R. Pathways to Structure-Property Relationships of Peptide-Materials Interfaces: Challenges in Predicting Molecular Structures. *Acc. Chem. Res.* **2017**, *7*, 1617–1624.

(98) Luo, Z.; Murello, A.; Wilkins, D. M.; Kovacik, F.; Kohlbrecher, J.; Radulescu, A.; Okur, H. I.; Ong, Q. K.; Roke, S.; Ceriotti, M.; Stellacci, F. Determination and evaluation of the nonadditivity in wetting of molecularly heterogeneous surfaces. *Proc. Natl. Acad. Sci. USA* **2019**, *116*, 25516–25523.

(99) Thomä, S. L. J.; Krauss, S. W.; Eckardt, M.; Chater, P.; Zobel, M. Atomic insight into hydration shells around facetted nanoparticles. *Nat. Comm.* **2019**, *10*, 995.

(100) Schrader, A. M.; Monroe, J. I.; Sheil, R.; Dobbs, H. A.; Keller, T. J.; Li, Y. X.; Jain, S.; Shell, M. S.; Israelachvili, J. N.; Han, S. Surface chemical heterogeneity modulates silica surface hydration. *Proc. Natl. Acad. Sci. USA* **2018**, *115*, 2890–2895.

(101) Breier, L. B.; Nagata, Y.; Lutz, H.; Gonella, G.; Hunger, J.; Backus, E. H. G.; Bonn, M. Saturation of charge-induced water alignment at model membrane surfaces. *Sci. Adv.* **2018**, *4*, eaap7415.

(102) Vacha, R.; Marsalek, O.; Willard, A. P.; Bonthuis, D. J.; Netz, R. R.; Jungwirth, P. Charge Transfer between Water Molecules As the Possible Origin of the Observed Charging at the Surface of Pure Water. *J. Phys. Chem. Lett.* **2012**, *3*, 107–111.

(103) Sakong, S.; Gross, A. The electric double layer at metal-water interfaces revisited based on a charge polarization scheme. *J. Chem. Phys.* **2018**, *149*, 084705.

(104) Kunz, W. Specific ion effects in colloidal and biological systems. *Curr. Opin Colloid Interf. Sci.* **2010**, *15*, 34–39.

(105) Cyran, J. D.; Donovan, M. A.; Vollmer, D.; Brigiano, F. S.; Pezzotti, S.; Galimberti, D. R.; Gaigeot, M. P.; Bonn, M.; Backus, E. H. G. Molecular hydrophobicity at

View Article Online
DOI: 10.1039/D0NR03792C

Published on 21 August 2020. Downloaded by Boston University on 8/21/2020 1:44:06 PM.

Nanoscale Accepted Manuscript

a macroscopically hydrophilic surface. *Proc. Natl. Acad. Sci. USA* **2019**, *116*, 1520–1525.

(106) Qiao, B. F.; Jimenez-Angeles, F.; Nguyen, T. D.; de la Cruz, M. O. Water follows polar and nonpolar protein surface domains. *Proc. Natl. Acad. Sci. USA* **2019**, *116*, 19274–19281.

(107) Dogangun, M.; Ohno, P. E.; Liang, D. Y.; McGeachy, A. C.; Dalchand, N.; Li, T.; Cui, Q.; Geiger, F. M. Hydrogen Bond Networks Near Supported Lipid Bilayers from Vibrational Sum Frequency Generation Experiments and Atomistic Simulations. *J. Phys. Chem. B* **2018**, *122*, 4870–4879.

(108) Sato, T.; Sasaki, T.; Ohnuki, J.; Umezawa, K.; Takano, M. Hydrophobic Surface Enhances Electrostatic Interaction in Water. *Phys. Rev. Lett.* **2018**, *121*, 206002.

(109) Loche, P.; Wolde-Kidan, A.; Schlaich, A.; Bonthuis, D. J.; Netz, R. R. Comment on “Hydrophobic Surface Enhances Electrostatic Interaction in Water”. *Phys. Rev. Lett.* **2019**, *123*, 049601.

(110) Ohnuki, J.; Sato, T.; Sasaki, T.; Umezawa, K.; Takano, M. Reply to Comment on “Hydrophobic Surface Enhances Electrostatic Interaction in Water”. *Phys. Rev. Lett.* **2019**, *123*, 049602.

(111) Zong, D.; Hu, H.; Duan, Y.; Sun, Y. Viscosity of water under electric field: Anisotropy induced by redistribution of hydrogen bonds. *J. Phys. Chem. B* **2016**, *120*, 4818–4827.

(112) Yeh, I.-C.; Berkowitz, M. L. Dielectric constant of water at high electric fields: Molecular dynamics study. *J. Chem. Phys.* **1999**, *110*, 7935–7942.

(113) Vorobyov, I.; Allen, T. W. The electrostatics of solvent and membrane interfaces and the role of electronic polarizability. *J. Chem. Phys.* **2010**, *132*, 05B602.

View Article Online
DOI: 10.1039/D0NR03792C

Published on 21 August 2020. Downloaded by Boston University on 8/21/2020 1:44:06 PM.

(114) McGeachy, A. C.; Caudill, E. R.; Liang, D.; Cui, Q.; Pedersen, J. A.; Geiger, F. M. Counting charges on membrane-bound peptides. *Chem. Sci.* **2018**, *9*, 4285–4298.

(115) Lund, M.; Jönsson, B. Charge Regulation in Biomolecular Solution. *Q. Rev. Biophys.* **2013**, *46*, 265–281.

(116) Gao, H. M.; Liu, H.; Zhang, R.; Lu, Z. Y. Structure Evolution of Binary Ligands on Nanoparticles Triggered by Competition between Adsorption Reaction and Phase Separation. *J. Phys. Chem. B* **2019**, *123*, 10311–10321.

(117) Jackson, A. M.; Myerson, J. W.; Stellacci, F. Spontaneous Assembly of Subnanometre-Ordered Domains in the Ligand Shell of Monolayer-Protected Nanoparticles. *Nat. Mater.* **2004**, *3*, 330–336.

(118) Luo, Z.; Marson, D.; Ong, Q. K.; Loiudice, A.; Kohlbrecher, J.; Radulescu, A.; Krause-Heuer, A.; Darwish, T.; Balog, S.; Buonsanti, R.; Svergun, D. I.; Posocco, P.; Stellacci, F. Quantitative 3D determination of self-assembled structures on nanoparticles using small angle neutron scattering. *Nat. Comm.* **2018**, *9*, 1343.

(119) Ghosh, P.; Verma, A.; Rotello, V. M. Binding and Templation of Nanoparticle Receptors to Peptide α-Helices through Surface Recognition. *Chem. Comm.* **2007**, *19*, 2796–2798.

Nanoscale Accepted Manuscript